

Emergence of curved momentum-spacetime and its effect on the cyclotron motion in the antiferromagnetic quantum critical metal

Francisco Borges^{1,2a} and Sung-Sik Lee^{1,2b}

¹*Department of Physics & Astronomy, McMaster University, Hamilton ON L8S 4M1, Canada and*

²*Perimeter Institute for Theoretical Physics, Waterloo ON N2L 2Y5, Canada*

(Dated: October 19, 2023)

We show that anisotropic quantum corrections can dynamically give rise to curved momentum-spacetimes for quasiparticles in metals. In the (2+1)-dimensional antiferromagnetic quantum critical metal, a curved momentum-spacetime arises as the critical spin fluctuations generate red shift that dilates frequency of electron unevenly on the Fermi surface. As the disparity of the momentum-dependent red shift is controlled by the shape of the Fermi surface, the momentum-spacetime geometry that emerges at low energies depends on the bare nesting angle of the Fermi surface. With increasing nesting angle, the region in which electron motion is slowed down by critical spin fluctuations shrinks. On the other hand, the increasing nesting angle makes the red shift stronger near the hot spots due to the weakened screening of the interaction. These competing effects result in a non-monotonic dependence of the cyclotron frequency of electron on the nesting angle of the Fermi surface. The red shift that becomes more singular at the hot spots with increasing nesting angle creates a possibility of realizing a momentum-space black hole horizon beyond a critical nesting angle : the electron motion becomes ‘perpetually’ slowed down as it approaches a hot spot in the same way that the motion of a free falling object freezes near the event horizon of a black hole with respect to an asymptotic observer. However, the analogous horizon in momentum space does not lead to a vanishing cyclotron frequency because the metric singularity at the hot spots is cut off by thermal effects present above the non-zero superconducting transition temperature.

I. Introduction

The semi-classical equation of motion of quasiparticles in solids is remarkably symmetric under the interchange of position and momentum. The momentum-dependent quasiparticle energy is the counter part of the position-dependent potential in real space. The Berry curvature associated with the Bloch wavefunctions plays the role of the magnetic field in momentum space[1]. It is then natural to ask if the symmetry can be further extended to spacetime geometry[2–6]. A real-space curvature can be created through buckling of lattices or topological defects in solids[7–15]. Recent studies on the semi-classical equations of motion of quasiparticles have suggested the emergence of a curved momentum space in lattice models. In particular, it has been pointed out that the non-linear response of quasiparticles to the external electromagnetic field can be captured geometrically[16, 17]. In those examples, the metric[18] is ultimately determined from the single-particle wavefunction fixed by the underlying lattice. In this paper, we consider an intrinsic physical mechanism by which momentum space and time is integrated into a curved *momentum-spacetime* through the electron-electron interactions. We point out that curved momentum-spacetimes naturally arise from anisotropic quantum corrections in metals and even a momentum-space black hole horizon can emerge if quantum corrections are strongly singular in momentum space.

Strongly momentum-dependent quantum corrections arise in metals close to quantum critical points associated with order parameters carrying non-zero momenta. At spin or charge density-wave critical points, electrons residing on hot manifolds, sub-manifolds of Fermi surface that can be connected by the ordering wave vectors, are more strongly scattered by critical fluctuations than electrons away from the hot manifolds. This leads to a momentum-dependent renormalization of electron. In particular, the Fermi velocity can acquire a strong dependence on momentum along the Fermi surface as electrons become significantly heavier near the hot manifold. Interestingly, a strongly momentum-dependent Fermi velocity can arise as a consequence of momentum-dependent red shift even without a direct renormalization of the band dispersion energy. Namely, the Fermi velocity can acquire momentum-dependence through a momentum-dependent dilatation of frequency : a quantum correction to the frequency-dependent kinetic term of electron is translated into a renormalization of the Fermi velocity. This momentum-dependent red shift is indeed the primary mechanism by which the Fermi velocity acquires a strong momentum dependence in the antiferromagnetic quantum critical metal in two space dimensions[19]. In such cases, one can understand phenomena associated with momentum-dependent Fermi velocity as consequences of a curved momentum-spacetime geometry. The same physics

^a fborges@perimeterinstitute.ca

^b slee@mcmaster.ca

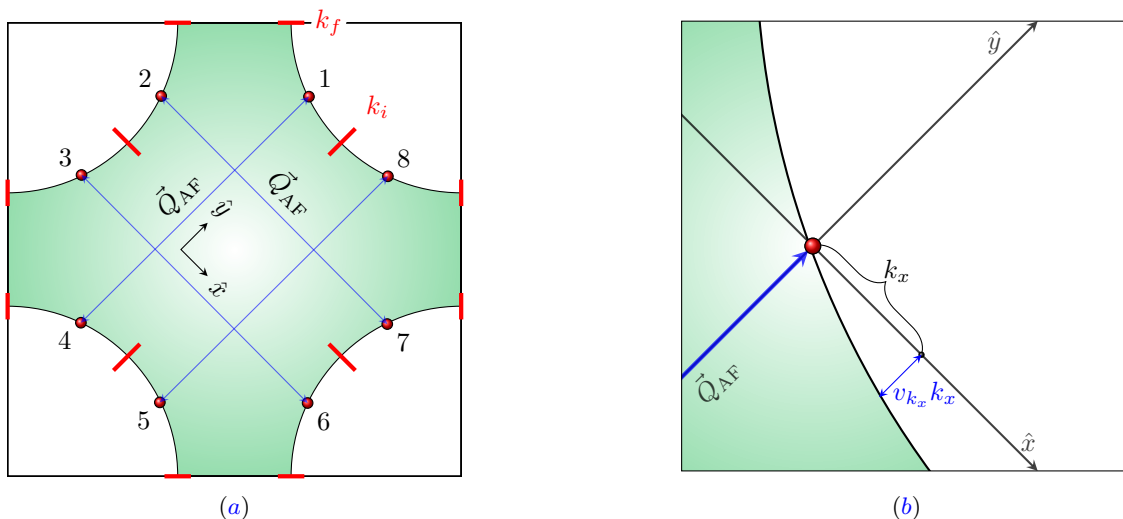


FIG. 1: For simplicity, we have omitted the superscript B in all the quantities in this figure. (a) The full Fermi surface divided into eight segments (separated by the red bars.) Segment 1 is bounded by k_i and k_f , and other segments are related to it through the C_4 and reflection symmetries. Each segment contains one hot spot denoted as red dots on the Fermi surface. The hot spots are connected by the antiferromagnetic ordering wave vector, \vec{Q}_{AF} . \hat{x} (\hat{y}) is chosen to be perpendicular (parallel) to \vec{Q}_{AF} at hot spot 1. (b) The Fermi surface in segment 1 is at $v_{k_x}k_x + k_y = 0$. Here, $v_{k_x}k_x$ represents the displacement of the Fermi surface from what the perfectly nested Fermi surface would have been.

can be understood without invoking a curved momentum-spacetime, just as the effects of curved spacetime in general relativity can be still described within the Newtonian framework. However, such non-geometric descriptions require introducing features that are rather arbitrary and finely tuned. For example, through the momentum-dependent red shift, only the magnitude of the Fermi velocity is renormalized even if the direction is not protected by generic quantum corrections that renormalize the Fermi velocity. In the geometric description, it is naturally captured as a renormalization of the temporal metric. For this reason, we adopt the geometric perspective to describe the dynamics of quasiparticles that are subject to momentum-dependent quantum corrections.

The antiferromagnetic quantum criticality is believed to play an important role in electron doped cuprates[20], iron pnictides[21], and heavy fermion compounds[22]. Although the theory in two space dimensions becomes strongly interacting at low energies, it has been non-perturbatively solved in the limit that the bare nesting angle is small[19, 23], building upon earlier works on the theory [24–45]. While electrons at the hot spots remain coupled with critical spin fluctuations down to the zero energy limit, electrons away from the hot spots are decoupled from spin fluctuations at sufficiently low energies. Since the crossover energy scale for the decoupling depends on momentum relative to the hot spots, quasiparticles are renormalized with a momentum-dependent red shift, which gives rise to a curved momentum-spacetime. If the momentum-dependent metric is singular enough, the emergent geometry can exhibit an analogous black hole horizon whose presence affects the dynamics of quasiparticles significantly. For example, the curved momentum-spacetime geometry could directly manifests itself in the cyclotron motion of quasiparticles. The effect of strong correlations on cyclotron mass enhancement has been the focus of many earlier works[46–56].

Here is the outline of the paper. In Sec. II, we review the field-theoretical functional renormalization group study of the antiferromagnetic quantum critical metal[19] with an emphasis on the results that are needed for the present work. In Sec. III, we cast the theory of the fully renormalized quasiparticles away from the hot spots into a theory of spinors propagating in a curved momentum-spacetime. In Sec. IV, we compute the cyclotron period of electron as a function of the bare nesting angle of the Fermi surface. We show that the unusual dependence of the cyclotron period on the nesting angle is a result of the non-trivial evolution of the curved momentum-spacetime geometry with varying nesting angle. We conclude with a summary and discussions in Sec. V.

II. The antiferromagnetic quantum critical metal in 2d

In this section, we first review the theory of the antiferromagnetic quantum critical metal in $2 + 1$ dimensions, focusing on the renormalized shape of the Fermi surface and the Fermi velocity that control the dynamics of low-

energy quasiparticles. In order to capture the momentum profiles of the coupling functions across the Fermi surface, we need to consider the low-energy effective field theory that includes all gapless modes on the Fermi surface[19],

$$\begin{aligned}
S = & \sum_{N=1}^8 \sum_{\sigma=1}^{N_c} \sum_{j=1}^{N_f} \int d\mathbf{k}^{\mathbf{B}} \psi_{N,\sigma,j}^{\mathbf{B}\dagger}(\mathbf{k}^{\mathbf{B}}) \left\{ ik_0^{\mathbf{B}} + V_{F,k_N^{\mathbf{B}}}^{\mathbf{B};(N)} e_N[\vec{k}^{\mathbf{B}}; v_{k_N^{\mathbf{B}}}^{\mathbf{B};(N)}] \right\} \psi_{N,\sigma,j}^{\mathbf{B}}(\mathbf{k}^{\mathbf{B}}) + \\
& \frac{1}{\sqrt{N_f}} \sum_{N=1}^8 \sum_{\sigma\sigma'=1}^{N_c} \sum_{j=1}^{N_f} \int d\mathbf{k}^{\mathbf{B}} d\mathbf{q}^{\mathbf{B}} g_{k_N^{\mathbf{B}}+q_N^{\mathbf{B}},k_N^{\mathbf{B}}}^{\mathbf{B};(N)} \psi_{N,\sigma',j}^{\mathbf{B}\dagger}(\mathbf{k}^{\mathbf{B}} + \mathbf{q}^{\mathbf{B}}) \Phi_{\sigma'\sigma}^{\mathbf{B}}(\mathbf{q}^{\mathbf{B}}) \psi_{N,\sigma,j}^{\mathbf{B}}(\mathbf{k}^{\mathbf{B}}) + \\
& \frac{1}{4} \sum_{\{N_i=1\}}^8 \sum_{\{\sigma_i=1\}}^{N_c} \sum_{\{j_i=1\}}^{N_f} \int \prod_{i=1}^4 d\mathbf{k}_i^{\mathbf{B}} \delta_{1+2,3+4}^{\mathbf{B}} \lambda^{\mathbf{B}; \left(\begin{smallmatrix} N_1 & N_2 \\ N_4 & N_3 \end{smallmatrix} \right); \left(\begin{smallmatrix} \sigma_1 & \sigma_2 \\ \sigma_4 & \sigma_3 \end{smallmatrix} \right)} \psi_{N_1,\sigma_1,j_1}^{\mathbf{B}\dagger}(\mathbf{k}_1^{\mathbf{B}}) \psi_{N_2,\sigma_2,j_2}^{\mathbf{B}\dagger}(\mathbf{k}_2^{\mathbf{B}}) \psi_{N_3,\sigma_3,j_3}^{\mathbf{B}}(\mathbf{k}_3^{\mathbf{B}}) \psi_{N_4,\sigma_4,j_4}^{\mathbf{B}}(\mathbf{k}_4^{\mathbf{B}}).
\end{aligned} \tag{1}$$

Here, we consider a Fermi surface with the C_4 and reflection symmetries that supports eight hot spots labelled by $N = 1, 2, \dots, 8$ as is shown in Fig. 1(a). The Fermi surface is divided into eight disjoint segments whose union covers the entire Fermi surface. Each segment, which contains one hot spot, is labelled by the associated hot spot index. $\psi_{N,\sigma,j}^{\mathbf{B}}(\mathbf{k}^{\mathbf{B}})$ represents the electron field in segment N with spin $\sigma = 1, 2, \dots, N_c$ and flavour $j = 1, 2, \dots, N_f$. The electron is in the fundamental representations of spin $SU(N_c)$ and flavour $SU(N_f)$ groups. The case that is most relevant to experiments is $N_c = 2$ and $N_f = 1$, but we keep N_c and N_f general because the solution obtained in the small nesting angle limit is valid for any $N_c \geq 2$ and $N_f \geq 1$. All quantities with superscript \mathbf{B} are bare ones in terms of which the microscopic theory is written. $d\mathbf{k}^{\mathbf{B}} \equiv \frac{dk_0^{\mathbf{B}} dk_x^{\mathbf{B}} dk_y^{\mathbf{B}}}{(2\pi)^3}$, where $\mathbf{k}^{\mathbf{B}} = (k_0^{\mathbf{B}}, \vec{k}^{\mathbf{B}}) = (k_0^{\mathbf{B}}, k_x^{\mathbf{B}}, k_y^{\mathbf{B}})$ denotes bare three-vector that includes the Matsubara frequency $k_0^{\mathbf{B}}$ and the two-dimensional momentum $\vec{k}^{\mathbf{B}}$ which is measured relative to the hot spot in each segment. The collective antiferromagnetic spin fluctuations are represented by a bosonic field $\Phi^{\mathbf{B}}(\mathbf{q}^{\mathbf{B}}) = \sum_{a=1}^{N_c^2-1} \phi^{\mathbf{B};a}(\mathbf{q}^{\mathbf{B}}) \tau^a$, where τ^a 's denote the $N_c \times N_c$ generators of $SU(N_c)$ with $\text{Tr}[\tau^a \tau^b] = 2\delta_{ab}$ and $\vec{q}^{\mathbf{B}}$ is measured relative to the ordering wavevector, \vec{Q}_{AF} . We consider the case where $2\vec{Q}_{AF}$ is equivalent to a reciprocal vector and $\phi^{\mathbf{B};a}(\mathbf{q}^{\mathbf{B}}) = \phi^{\mathbf{B};a}(-\mathbf{q}^{\mathbf{B}})^*$. The momentum conserving delta function is denoted as $\delta_{1+2,3+4}^{\mathbf{B}} \equiv (2\pi)^3 \delta(\mathbf{k}_1^{\mathbf{B}} + \mathbf{k}_2^{\mathbf{B}} - \mathbf{k}_3^{\mathbf{B}} - \mathbf{k}_4^{\mathbf{B}})$. $k_N^{\mathbf{B}}$ represents the component of momentum that labels the Fermi surface in segment N ,

$$k_N^{\mathbf{B}} = \begin{cases} k_x^{\mathbf{B}} & \text{for } N = 1, 4, 5, 8 \\ k_y^{\mathbf{B}} & \text{for } N = 2, 3, 6, 7 \end{cases}.$$

\bar{N} represents the hot spot connected to N by the ordering vector \vec{Q}_{AF} ; for example, $\bar{N} = 4$ for $N = 1$. Although neither \hat{x} nor \hat{y} direction is perfectly parallel to the Fermi surface in general, there is one-to-one correspondence between $k_N^{\mathbf{B}}$ and a point on the Fermi surface in each segment. $V_{F,k_N^{\mathbf{B}}}^{\mathbf{B};(N)}$ is the bare momentum-dependent Fermi velocity in the direction parallel to \vec{Q}_{AF} in segment N . It is the ‘‘bare’’ coupling because is the cutoff-dependent value in the action indicating the starting point where the RG flow will begin to run from. $e_N[\vec{k}^{\mathbf{B}}, v_{k_N^{\mathbf{B}}}^{\mathbf{B};(N)}]$ specifies the Fermi surface in segment N through

$$\begin{aligned}
e_1[\vec{k}^{\mathbf{B}}; v_{k_x^{\mathbf{B}}}^{\mathbf{B};(1)}] &= v_{k_x^{\mathbf{B}}}^{\mathbf{B};(1)} k_x^{\mathbf{B}} + k_y^{\mathbf{B}}, & e_2[\vec{k}^{\mathbf{B}}; v_{k_y^{\mathbf{B}}}^{\mathbf{B};(2)}] &= -v_{k_y^{\mathbf{B}}}^{\mathbf{B};(2)} k_y^{\mathbf{B}} - k_x^{\mathbf{B}}, \\
e_3[\vec{k}^{\mathbf{B}}; v_{k_y^{\mathbf{B}}}^{\mathbf{B};(3)}] &= v_{k_y^{\mathbf{B}}}^{\mathbf{B};(3)} k_y^{\mathbf{B}} - k_x^{\mathbf{B}}, & e_4[\vec{k}^{\mathbf{B}}; v_{k_x^{\mathbf{B}}}^{\mathbf{B};(4)}] &= v_{k_x^{\mathbf{B}}}^{\mathbf{B};(4)} k_x^{\mathbf{B}} - k_y^{\mathbf{B}}, \\
e_5[\vec{k}^{\mathbf{B}}; v_{k_x^{\mathbf{B}}}^{\mathbf{B};(5)}] &= -v_{k_x^{\mathbf{B}}}^{\mathbf{B};(5)} k_x^{\mathbf{B}} - k_y^{\mathbf{B}}, & e_6[\vec{k}^{\mathbf{B}}; v_{k_y^{\mathbf{B}}}^{\mathbf{B};(6)}] &= v_{k_y^{\mathbf{B}}}^{\mathbf{B};(6)} k_y^{\mathbf{B}} + k_x^{\mathbf{B}}, \\
e_7[\vec{k}^{\mathbf{B}}; v_{k_y^{\mathbf{B}}}^{\mathbf{B};(7)}] &= -v_{k_y^{\mathbf{B}}}^{\mathbf{B};(7)} k_y^{\mathbf{B}} + k_x^{\mathbf{B}}, & e_8[\vec{k}^{\mathbf{B}}; v_{k_x^{\mathbf{B}}}^{\mathbf{B};(8)}] &= -v_{k_x^{\mathbf{B}}}^{\mathbf{B};(8)} k_x^{\mathbf{B}} + k_y^{\mathbf{B}}.
\end{aligned} \tag{2}$$

If $v_{k_N^{\mathbf{B}}}^{\mathbf{B};(N)} = 0$, pairs of segments connected by \vec{Q}_{AF} become perfectly nested. In general, $v_{k_N^{\mathbf{B}}}^{\mathbf{B};(N)}$ is non-zero and $k^{\mathbf{B}}$ -dependent. For this reason, we call $v_{k_N^{\mathbf{B}}}^{\mathbf{B};(N)}$ the bare momentum-dependent nesting angle. The full Fermi velocity vector in term of $V_{F,k_N^{\mathbf{B}}}^{\mathbf{B};(N)}$ and $v_{k_N^{\mathbf{B}}}^{\mathbf{B};(N)}$ is given by

$$\vec{v}_F^{\mathbf{B}}(k_x^{\mathbf{B}}) = V_{F,k_x^{\mathbf{B}}}^{\mathbf{B};(1)} \left(\frac{\partial v_{k_x^{\mathbf{B}}}^{\mathbf{B};(1)}}{\partial k_x^{\mathbf{B}}} k_x^{\mathbf{B}} + v_{k_x^{\mathbf{B}}}^{\mathbf{B};(1)} \right) \hat{x} + V_{F,k_x^{\mathbf{B}}}^{\mathbf{B};(1)} \hat{y}, \tag{3}$$

where $N = 1$ (See Fig. 1(b).) The Yukawa coupling denoted as $g_{k'^B, k^B}^{B;(N)}$ is a function of initial and final momenta of electrons. Similarly, $\lambda_{\begin{pmatrix} N_1 & N_2 \\ N_4 & N_3 \end{pmatrix}; \begin{pmatrix} \sigma_1 & \sigma_2 \\ \sigma_4 & \sigma_3 \end{pmatrix}}^{B;}$ denotes the short-range four-fermion interaction labelled by momenta of electrons on the Fermi surface. The coupling functions in different segments are related to each other through symmetry, and $v_{k^B}^{B;(N)}$, $V_{F, k^B}^{B;(N)}$ and $g_{k'^B, k^B}^{B;(N)}$ can be written as

$$\left(v_{k^B}^{B;(N)}, V_{F, k^B}^{B;(N)}, g_{k'^B, k^B}^{B;(N)} \right) = \begin{cases} \left(v_{k^B}^B, V_{F, k^B}^B, g_{k'^B, k^B}^B \right), & N = 1, 3, 4, 6 \\ \left(v_{-k^B}^B, V_{F, -k^B}^B, g_{-k'^B, -k^B}^B \right), & N = 2, 5, 7, 8 \end{cases}. \quad (4)$$

Similarly, four-fermion coupling functions that are mapped to each other under the symmetry are related. Under Gaussian scaling, in which the kinetic terms are kept invariant, the Yukawa coupling has scaling dimension $[g] = 1/2$. The perturbative expansion is organized in powers of $g/E^{1/2}$ at energy scale E , and becomes uncontrolled at low energies. Fortunately, the theory can be solved non-perturbatively in the limit that the nesting angle is small. The interacting low-energy fixed point obeys a new scaling relation[57] in which the boson acquires an $O(1)$ anomalous dimension. At the interacting fixed point, the Yukawa coupling becomes marginal while the local bosonic kinetic term is irrelevant. This is why the boson kinetic term is not included in Eq. (1). The details of the non-perturbative solution can be found in Refs. [19, 23]. In the remaining of this section, we recap the results that are needed for this paper.

Physical observables such as the correlation functions of the theory are fully encoded in the one-particle irreducible vertex functions. We denote the vertex function of $2m$ fermions and n bosons as $\Gamma^{(2m, n)}(\mathbf{k}_1, \dots, \mathbf{k}_{2m+n-1})$, where \mathbf{k}_i represents the energy-momentum vector of the i -th particle. The vertex functions are defined in terms of renormalized fields $\psi_{N, \sigma, j}$ and $\Phi_{\sigma', \sigma}$, which are related to the bare fields through multiplicative field renormalization factors[19]. All variables without superscript B are renormalized quantities. Renormalized frequency and momentum can be also related to the bare ones. Here, we use $\vec{k} = \vec{k}^B$. However, the renormalized frequency is chosen to be related to the bare frequency through a non-linear scale transformation, $k_0^B = k_0 e^{-\int_{k_0}^{\Lambda} dk'_0 z_\tau(k'_0)}$, where $z_\tau(k'_0)$ is the scale-dependent dynamical critical exponent and Λ is the scale at which the bare and renormalized frequencies coincide. In principle, we can rescale frequency however we want, but it is convenient to choose the dynamical critical exponent such that the renormalized Fermi velocity at the hot spots is fixed to be 1 when measured with the renormalized frequency[19, 23]. The set of momentum and energy dependent vertex functions that control all other vertex functions is related to the

coupling functions $\left\{ v_k, V_{F, k}, g_{k', k}, \lambda_{\begin{pmatrix} N_1 & N_2 \\ N_4 & N_3 \end{pmatrix}; \begin{pmatrix} \sigma_1 & \sigma_2 \\ \sigma_4 & \sigma_3 \end{pmatrix}}^{B;}, \lambda_{\begin{pmatrix} k_{1; N_1} & k_{2; N_2} \\ k_{4; N_4} & k_{3; N_3} \end{pmatrix}}^{B;} \right\}$. In this paper, we only need the momentum-dependent nesting angle v_k and Fermi velocity $V_{F, k}$ defined through

$$\left. \text{Re} \Gamma_1^{(2, 0)}(\mathbf{k}) \right|_{\mathbf{k}=(\mu, k_x, -v_{k_x} k_x)} = 0, \quad \left. \frac{\partial}{\partial k_y} \text{Re} \Gamma_1^{(2, 0)}(\mathbf{k}) \right|_{\mathbf{k}=(\mu, k_x, -v_{k_x} k_x)} = V_{F, k_x}, \quad (5)$$

where $\Gamma_N^{(2, 0)}(\mathbf{k})$ is the two-point vertex function for electron in segment N . The first equation in Eq. (5) should be viewed as the defining equation for the renormalized nesting angle v_k that determines the shape of the Fermi surface at renormalized frequency μ . The second equation defines the renormalized Fermi velocity through the vertex function evaluated on the Fermi surface. Once the shape and Fermi velocity are fixed in segment 1, the symmetry fix them in all other segments. The field renormalization of electron and the dynamical critical exponent are chosen such that

$$\left. \frac{\partial}{\partial k_0} \text{Im} \Gamma_1^{(2, 0)}(\mathbf{k}) \right|_{\mathbf{k}=(\mu, k_x, -v_{k_x} k_x)} = i \text{ and } V_{F, 0} = 1.$$

To simplify the notation, from now on we will use k and k_x interchangeably. The evolution of v_k and $V_{F, k}$ with decreasing μ defines the functional renormalization group flow[19]. Below, we will use $\ell \equiv \log \Lambda / \mu$ to denote the logarithmic length scale that increases as the low-energy limit is taken, where Λ is a UV cutoff energy scale. In the small nesting angle limit, the self-energy that determines the renormalization of v_k and $V_{F, k}$ can be computed. For the full details, see Appendix A and Sec. VI of Ref. [19]. In the space of coupling functions, the theory supports an *interacting* fixed point[19, 23] at which the anomalous dimension of the boson is $O(1)$. As the theory flows toward the fixed point, the coupling functions acquire non-trivial momentum dependence due to the momentum-dependent quantum corrections. In this paper, we consider the case in which the coupling functions are independent of momentum at the UV energy scale: $v_k(\ell = 0) = v_0(0)$, $V_{F, k}(\ell = 0) = 1$. Different choices of UV couplings do not change the universal singularities of the renormalized coupling functions that play the important role as we will see later.

Electrons on the Fermi surface receive quantum corrections in a momentum-dependent manner because electrons away from the hot spots are decoupled from spin fluctuations below a momentum-dependent crossover energy scale. The crossover scale is given by $E_k^{(2L)} \equiv \Lambda e^{-\ell_k^{(2L)}}$ (see Appendix A for more details), where

$$\ell_k^{(2L)} = \log\left(\frac{\Lambda}{4V_{F,k}v_k|k|}\right) \quad (6)$$

denotes the logarithmic length scale associated with the crossover. This crossover occurs because electrons away from hot spots can not interact with with critical spin fluctuations with zero energy while staying on the Fermi surface due to a lack of the perfect nesting for $v_k \neq 0$. Here, we emphasize that v_k is small but non-zero in the non-perturbative solution. This momentum-dependent crossover creates two *momentum scales*, $k_c(\ell)$ and $k_h(\ell)$ determined from $\ell_{k_c}^{(2L)} = 0$ and $\ell_{k_h}^{(2L)} = \ell$, respectively. They divide the momentum space into three regions at a finite length scale ℓ . To the leading order in v_k , these momentum scales can be approximated as $k_c \approx \frac{\Lambda}{4v_0(0)}$ and $k_h \approx \frac{\Lambda e^{-\ell}}{4v_0(0)}$. In the ‘cold’ region with $k > k_c$, electrons are too far away from the hot spot to receive significant quantum correction at energies below Λ . In the ‘lukewarm’ region with $k_h(\ell) < k < k_c$, electrons receive non-trivial quantum corrections between Λ and $E_k^{(2L)}$. But, the electrons in the lukewarm region are largely decoupled from spin fluctuations at energy scale ℓ . In the ‘hot’ region with $k < k_h(\ell)$, electrons remain strongly coupled with critical spin fluctuations at scale ℓ . This gives rise to the following momentum profiles for the renormalized nesting angle v_k and Fermi velocity $V_{F,k}$ [19] at scale ℓ ,

$$v_k = \begin{cases} \frac{\ell_0 \log(\ell_0)}{(\ell + \ell_0) \log(\ell + \ell_0)} v_0(0) & 0 \leq k < k_h \\ \frac{\ell_0 \log(\ell_0)}{(\ell_k^{(2L)} + \ell_0) \log(\ell_k^{(2L)} + \ell_0)} v_0(0) & k_h \leq k < k_c, \\ v_0(0) & k_c \leq k \end{cases}, \quad (7)$$

$$V_{F,k} = \begin{cases} 1 & 0 \leq k < k_h \\ \exp\left(\sqrt{N_c^2 - 1} \left(\text{Ei}(\log \sqrt{\ell + \ell_0}) - \text{Ei}(\log \sqrt{\ell_k^{(2L)} + \ell_0}) \right)\right) & k_h \leq k < k_c. \\ \exp\left(\sqrt{N_c^2 - 1} \left(\text{Ei}(\log \sqrt{\ell + \ell_0}) - \text{Ei}(\log \sqrt{\ell_0}) \right)\right) & k_c \leq k \end{cases}. \quad (8)$$

Here, $\text{Ei}(x)$ is the exponential integral function and

$$\ell_0 = \frac{\pi^2 N_c N_f}{2(N_c^2 - 1)} \frac{1}{v_0(0) \log(1/v_0(0))} \quad (9)$$

represents the logarithmic length scale below which the flow of the nesting angle is negligible. We emphasize that the nesting angle and Fermi velocity acquire the non-trivial momentum dependence at low energies even if they are independent of momentum at the UV scale. The nesting angle is unchanged for $k \geq k_c$ because the Fermi surface is not renormalized far away from the hot spots. As k decreases in the lukewarm region, the nesting angle decreases logarithmically in k as spin fluctuations mix electrons in segments with opposite orientations. The nesting angle reaches the smallest value in $k < k_h$. The nesting angle right at the hot spot continues to decrease with increasing ℓ . On the other hand, the Fermi velocity is 1 for $k \leq k_h$ at all energy scale. As discussed earlier, this is the consequence of the frequency rescaling where the renormalized frequency is chosen such that the Fermi velocity is one at the hot spots. The price that we pay for this choice is that the Fermi velocity increases with increasing k in the lukewarm and cold regions. The Fermi velocity in the cold region keep increasing with increasing ℓ despite the fact that they are not renormalized by spin fluctuations. What really happens is that electrons in the the hot region are slowed down by spin fluctuations while electrons in the cold region are not. In the unit of time in which the the Fermi velocity is fixed to be 1 at the hot spots, the electrons away from the hot spots acquire Fermi velocity that keep increasing in the low-energy limit.

As ℓ increases, the size of hot region shrinks as more electrons become decoupled from spin fluctuations. In the strict zero temperature limit, the theory develops superconducting instabilities due to the run-away flow of the four-fermion coupling function[19]. However, the normal state remains stable down to an energy scale that is exponentially small in $1/\sqrt{v_0(0)}$ in the limit that $v_0(0)$ is small and the bare four-fermion coupling is weak. Here, we study the dynamics of electrons at energies low enough that electrons are decoupled from the critical spin fluctuations almost everywhere on the Fermi surface except for the immediate vicinity of the hot spots but high enough that the superconducting instability is absent. As a first step, we consider the dynamics of quasiparticles at zero temperature, ignoring the superconducting instability. Later, we consider the thermal effect that arises above the superconducting transition temperature.

III. Emergence of a curved momentum-spacetime

At zero energy ($\ell = \infty$) the Fermi velocity away from the hot spots becomes infinite. This represents the fact that electrons at the hot spots becomes infinitely slower than the rest of electrons. While the choice of the renormalized frequency is convenient for describing the scaling behaviour of electrons at the hot spots and the critical spin fluctuations[23], it is not useful for describing the dynamics of electrons away from the hot spots. For electrons away from hot spots, it is more convenient to use the bare clock with respect to which the velocity of the cold electrons is fixed to be 1. We can go back to the bare unit of frequency by undoing the rescaling the frequency as

$$k_0 = \left(\frac{V_{F,k_c}^{(N)}}{V_{F,0}^{(N)}} \right) \omega, \quad \psi_{N,\sigma,j}(\mathbf{k}) = \left(\frac{V_{F,k_c}^{(N)}}{V_{F,0}^{(N)}} \right)^{-1} \tilde{\psi}_{N,\sigma,j}(\omega, \vec{k}), \quad (10)$$

where we use $\omega \equiv k_0^{\text{B}}$ for simplicity of notation, and the normalization of the field is chosen to keep the canonical form of the quantum effective action,

$$\Gamma_{\text{kin}} = \sum_{N=1}^8 \sum_{\sigma=1}^{N_c} \sum_{j=1}^{N_f} \int \frac{d\omega d^2\vec{k}}{(2\pi)^3} \tilde{\psi}_{N,\sigma,j}^\dagger(\omega, \vec{k}) \left\{ i\omega + \mathcal{V}_{F,k_N}^{(N)} e_N \left[\vec{k}; v_{k_N}^{(N)} \right] \right\} \tilde{\psi}_{N,\sigma,j}(\omega, \vec{k}). \quad (11)$$

For the rest of the paper, we will use the bare frequency. Here, $\mathcal{V}_{F,k_N}^{(N)} = \left(\frac{V_{F,0}^{(N)}}{V_{F,k_c}^{(N)}} \right) V_{F,k_N}^{(N)}$ denotes the Fermi velocity measured in the bare time.

In the low-energy limit, k_h approaches zero and the hot region shrinks to points. This implies that quasiparticles are well defined everywhere on the Fermi surface except at the hot spots. The dynamics of the fully renormalized quasiparticles is described by the quadratic action¹ in Eq. (11) with nesting angle v_k and Fermi velocity (along \vec{Q}_{AF}) $\mathcal{V}_{F,k}$ given by

$$v_k = \begin{cases} \frac{\pi^2 N_c N_f}{2(N_c^2 - 1)} \frac{1}{(\ell_k^{(2L)} + \ell_0) \log(\ell_k^{(2L)} + \ell_0)} & 0 \leq k < k^* \\ v_0(0) & k^* \leq k \end{cases} \quad \text{and} \quad \mathcal{V}_{F,k} = \begin{cases} e^{\sqrt{N_c^2 - 1} \left(-\text{Ei}(\log \sqrt{\ell_k^{(2L)} + \ell_0}) + \text{Ei}(\log \sqrt{\ell_0}) \right)} & 0 \leq k < k^* \\ \left(\frac{k}{k_c} \right)^{\alpha_1} & k^* < k < k_c \\ 1 & k_c \leq k \end{cases}, \quad (12)$$

respectively, where $k^* = \frac{\Lambda e^{-\ell_0}}{4v_0(0)}$ is the momentum scale below which the flow of the nesting angle is appreciable and is determined from $\ell_0 = \ell_{k^*}^{(2L)}$. It is noted that the renormalized nesting angle in Eq. (7) can be well approximated to be $v_0(0)$ for $k > k^*$ in the limit that $v_0(0)$ is small (equivalently $\ell_0 \gg 1$).

$$\alpha_1 = \frac{\sqrt{N_c - 1}}{\sqrt{\ell_0} \log \ell_0} \quad (13)$$

is the critical exponent of the Fermi velocity. As expected in Eq. (12), $\mathcal{V}_{F,k} = 1$ for $k > k_c$ and vanishes at the hot spots. There are two noteworthy features in Eq. (12). First, in $k^* < k < k_c$, $\mathcal{V}_{F,k}$ scales with k algebraically while v_k is almost constant. This is because the quantum correction that renormalizes $\mathcal{V}_{F,k}$ is stronger than what renormalizes v_k [19]. As a result, v_k is almost momentum-independent except in the vicinity of the hot spot within $k < k^*$, as expressed in Eq. (12) for v_k . Second, with virtually k -independent v_k in $k > k^*$, both x and y components of Fermi velocity are renormalized in the same fashion although there is no symmetry that protects the direction of the Fermi velocity. This peculiarity arises because the dominant renormalization of Fermi velocity is from the quantum correction to the frequency-dependent (ik_0) term of the action in Eq. (1)[19]. In other words, the momentum dependence of $\mathcal{V}_{F,k}$ arises because the strength of the quantum correction that dilates frequency depends on momentum along the Fermi surface. In the scheme that uses one global clock for the entire system, we are forced to transfer the momentum dependence of the quantum correction to the field renormalization and Fermi velocity. While this is a perfectly legitimate picture, what the theory is really suggesting is to view the momentum-dependent Fermi velocity as a

¹ Besides the quadratic action, there also exists the four-fermion coupling that has been generated by the critical spin fluctuations. However, their effects on the quasiparticle motion is sub-leading compared to the quantum corrections that have been already incorporated into v_k and $\mathcal{V}_{F,k}$ in the limit that the nesting angle is small.

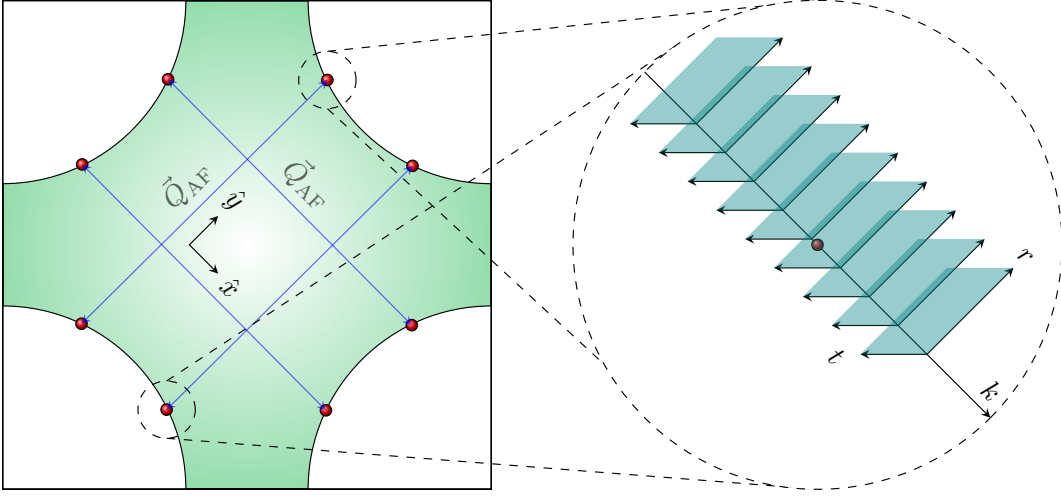


FIG. 2: The spinor composed of the electrons in segments 1 and 5 is defined in the hybrid spacetime (t, r, k) , where t is time, r is space conjugate to k_y and $k = k_x$. At fixed k , electrons at hot spots 1 and 5 have the same dynamics due to the time-reversal symmetry, and can be naturally described by the two-component spinor Ψ in Eq. (14).

consequence of non-uniform temporal metric on the Fermi surface. Here, we adopt this perspective in which electrons have momentum-independent Fermi velocity in $k^* < k < k_c$ once the velocity is measured with a proper time defined with respect to a momentum-dependent metric.

We formulate this geometric description by casting Eq. (11) into a theory of quasiparticles propagating in a curved spacetime that incorporates the momentum-dependent metric. For a brief review of the fermionic action defined in curved spacetime, see Appendix B. For our particular case, we view the Fermi surface as a collection of 1 + 1-dimensional Dirac fermions stacked along the direction of Fermi surface, and combine a pair of chiral fermions at anti-podal points of the Fermi surface into a two-component Dirac spinor[58]. Let us focus on segments 1 and 5 in this representation. Electrons in these anti-podal hot spots can be naturally paired since they have the same dynamics (See Fig. 1.) The two-component spinor is given by the Fourier transform

$$\Psi_{\sigma,j}(t, r, k_x) \equiv \int \frac{d\omega dk_y}{(2\pi)^2} e^{i(\omega t + k_y r)} \begin{bmatrix} \psi_{1,\sigma,j}(\omega, k_x, k_y) \\ \psi_{5,\sigma,j}^*(-\omega, -k_x, -k_y) \end{bmatrix}. \quad (14)$$

Here, the hot spot index is dropped as we focus on $N = 1$ and 5 (it is straightforward to write down the theory for other segments.) The theory is written in the hybrid spacetime of (t, r, k) [57], where t is time, r is the conjugate variable of k_y , and $k = k_x$ labels points on the Fermi surface in segments 1 and 5 (See Fig. 2.) From Eq. (14), it is straightforward to write the action in Eq. (11) for segments 1 and 5 in the hybrid space of t, r, k_x . The resulting action in terms of the spinors is

$$\Gamma_{\text{kin}}^{(1,5)} = \sum_{\sigma=1}^{N_c} \sum_{j=1}^{N_f} \int \frac{dk}{2\pi} \int dt dr |\epsilon| \bar{\Psi}_{\sigma,j}(t, r, k) \{ \gamma^0 \epsilon_0^t D_t + \gamma^1 \epsilon_1^r D_r \} \Psi_{\sigma,j}(t, r, k), \quad (15)$$

where $\bar{\Psi} = \Psi^\dagger \gamma^0$, where $\gamma^0 = \sigma_y$, $\gamma^1 = \sigma_x$, $\gamma^2 = \sigma_z$ denote 2×2 gamma matrices that furnish the two-dimensional spinor representation. ϵ_a^μ is the inverse of the vielbein e_μ^a with $a = 0, 1, 2$ and $\mu = t, r, k$. The vielbein determines the metric in the 2 + 1-dimensional spacetime through $g_{\mu\nu} = \sum_{a=0}^2 e_\mu^a e_\nu^a$. In general, the vielbein is a function of t, r, k , but in our case it depends only on k : $\epsilon_0^t(k) = \mathcal{V}_{F,k}$, $\epsilon_1^r(k) = \epsilon_k^2(k) = 1$ with all other elements being zero. $|\epsilon|$ is the determinant of e_μ^a . $D_\mu = \partial_\mu + \frac{i}{2} \omega_{\mu,ab} \Sigma^{ab} + i A_\mu$ denotes the covariant derivative, where $\omega_{\mu,ab}$ is the spin connection with $\Sigma^{ab} = \frac{i}{4} [\gamma^a, \gamma^b]$ and A_μ is the U(1) gauge field. Eq. (15) becomes equivalent to Eq. (11) for the trivial spin connection $\omega_{\mu,ab} = 0$ and the gauge field given by $A_t = 0$, $A_r = v_k k$, $A_k = 0$. The gauge field A_r gives a k_x -dependent shift of momentum in the r direction so that quasiparticles have zero energy at $k_y = -v_{k_x} k_x$.

Eq. (15) describes quasiparticles moving in a curved hybrid spacetime with a non-trivial torsion. It expresses the fact that the Fermi velocity along the direction of \vec{Q}_{AF} is 1 everywhere on the Fermi surface if the momentum-dependent proper time interval $d\tau = \epsilon_0^t(k) dt$ is used in measuring velocity at momentum k . The ‘apparent’ variation

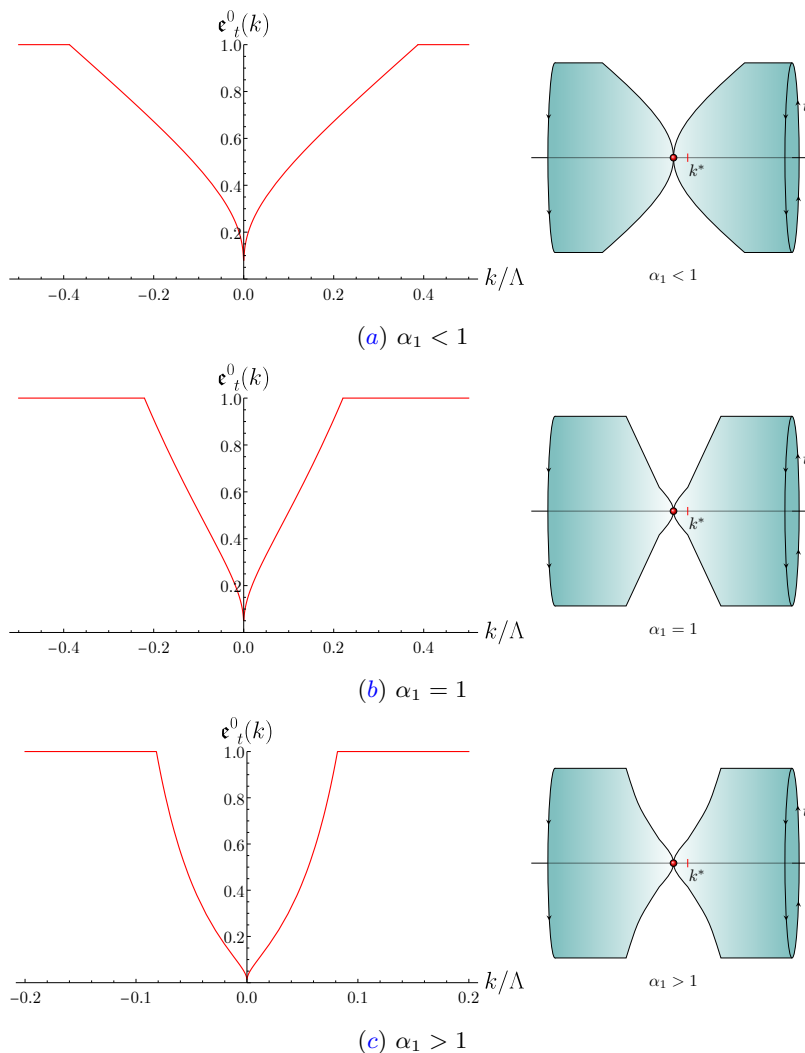


FIG. 3: The vielbein $\epsilon_t^0(k)$ that depends on momentum along the Fermi surface determines the rate at which the proper time lapses at momentum k per unit proper time of cold electrons far away from the hot spots. The vielbein that vanishes at the hot spots represents the fact that the motion of electrons at the hot spots become infinitely slowed down compared to cold electrons. (Left) The momentum-dependent vielbein ϵ_t^0 for (a) $\alpha_1 \approx 0.663$, (b) $\alpha_1 \approx 1$ and (c) $\alpha_1 \approx 2.169$. The choice in (b) corresponds to the critical nesting angle at which the cyclotron period exhibits a logarithmic dependence on momentum (see Eq. (22)). (Right) The $t-k$ slice of the hybrid spacetime for fixed r . For the purpose of illustrating the momentum-dependence of the vielbein, the temporal coordinate has been compactified so that the size of the circumference at each k represents the proper time lapsed at that momentum for every unit proper time of cold electrons. The circumference pinches off at the hot spots due to the infinitely large red shift at those points.

of Fermi velocity along the Fermi surface arises only when one chooses to probe the dynamics of quasiparticles in one fixed clock. For an external lab observer whose clock ticks once for every unit proper time defined in $k > k_c$, quasiparticles appear to slow down near hot spots due to the momentum-dependent red-shift in the same way that a free falling object appears to undergo a slower time evolution near the surface of a massive object with respect to the far observer due to the gravitational red shift.

The $t-k$ slice of the momentum-spacetime is illustrated in Fig. 3 for the case in which the temporal direction is compact. In $k \gg k_c$, the proper length of the temporal direction remains equal to the periodicity of t since $\epsilon_t^0 = 1$. In $k^* < k < k_c$, the proper length scales with k algebraically with exponent α_1 ($\epsilon_t^0 \sim k^{\alpha_1}$). Hence, the proper time lapses slower as the hot spot is approached. In $k < k^*$, the power-law decay is replaced with a slower decay due to a flow of the nesting angle as is shown in Eq.(12).

With the vielbein and spin connection fully fixed by the renormalized coupling functions, Cartan's structure equation

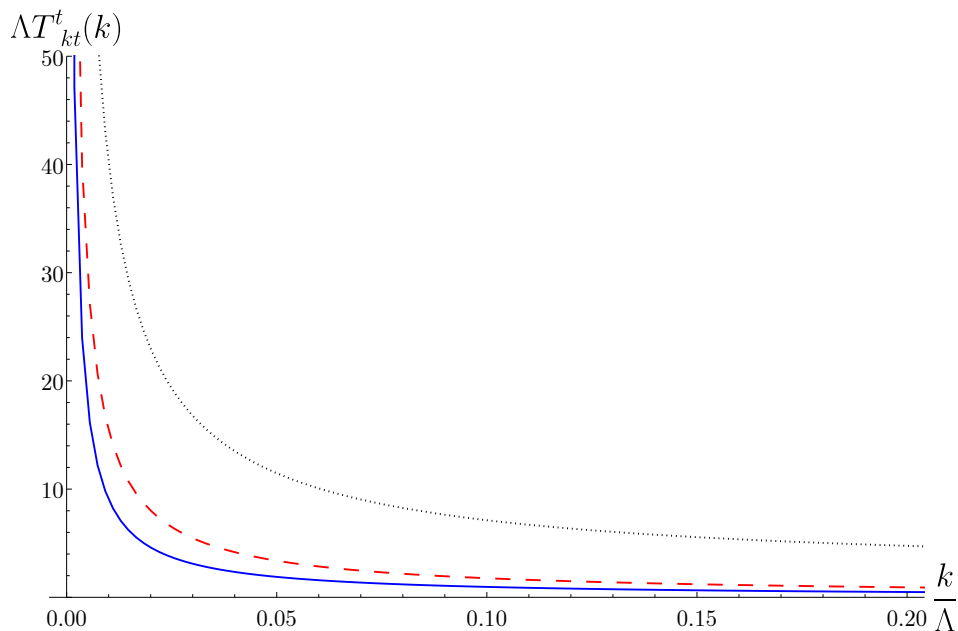


FIG. 4: The non-zero component of torsion shown as a function of momentum along the Fermi surface near the hot spots. The torsion, as a gauge-invariant geometric quantity, represents how much the momentum-spacetime in which quasiparticles propagate has been distorted from the flat one that arises in the absence of momentum-dependent quantum corrections. The plot is obtained from $\frac{1}{\epsilon_t^0} \frac{d\epsilon_t^0}{dk}$ by substituting Eq. (12) into ϵ_t^0 , and with the help of Eqs. (6), (9), and (13). The solid blue, dashed red and dotted black curves correspond to $v_0(0) \approx 0.04$, $v_0(0) \approx 0.13$ and $v_0(0) \approx 1.13$, respectively. This shows that the spacetime is more strongly distorted near the hot spots and for larger bare nesting angles.

determines the torsion of the spacetime to be $T^t = \frac{1}{\epsilon_t^0} \frac{d\epsilon_t^0}{dk} dk \wedge dt$, $T^r = T^k = 0$. The torsion measures the failure of closure when each of two vector is parallel transported along the other vector. The non-zero component of the torsion indicates a non-trivial structure of the hybrid spacetime. For the present hybrid spacetime, the torsion diverges in the $k \rightarrow 0$ limit as is shown in Fig. 4. In principle, the torsion can be measured from the rate at which the red shift varies along the Fermi surface. However, it is not clear how the momentum-dependent torsion can be directly measured from an experimental probe that is local in momentum space. Here, we consider a physical observable that probes the global aspect of the distorted momentum-spacetime, which is sensitive to the torsion yet much easier to measure experimentally.

IV. Cyclotron motion of quasiparticles in the curved momentum-spacetime

In this section, we examine how the curved momentum-spacetime affects the dynamics of quasiparticles by computing the cyclotron period of electron in the presence of magnetic field[59, 60]. Due to the C_4 symmetry and the reflection symmetry around the boundary between segments, the cyclotron period at bare nesting angle v_0 ² is eight times the time it takes for a quasiparticle to traverse segment 1 : $T(v_0) = 8 [T(k_i, 0; v_0) + T(0, k_f; v_0)]$, where $T(k_i, 0; v_0)$ denotes the time that it takes for a quasiparticle to traverse from the boundary between segments 1 and 8 to hot spot 1, and $T(0, k_f; v_0)$, from hot spot 1 to the Brillouin zone boundary between segments 1 and 6 (see Fig. 1). The setup is depicted in Fig. 5. For simplicity, we assume $T(0, k_f; v_0) = T(k_i, 0; v_0)$ and focus on the computation of $T(k_i, 0; v_0)$ here³.

In the zero temperature limit, well-defined quasiparticles exist away from the hot spots and we can use the semi-classical description of their dynamics. Strictly speaking, electrons right at the hot spots are not described by

² In this section, we use v_0 and $v_0(0)$ interchangeably for the momentum-independent bare nesting angle.

³ In general, $T(0, k_f; v_0) \neq T(k_i, 0; v_0)$ because there is no reflection symmetry around the hot spots. However, the computation of $T(0, k_f; v_0)$ is exactly parallel to that of $T(k_i, 0; v_0)$. This is because the singular part of the quantum corrections are symmetric around the hot spots[19].

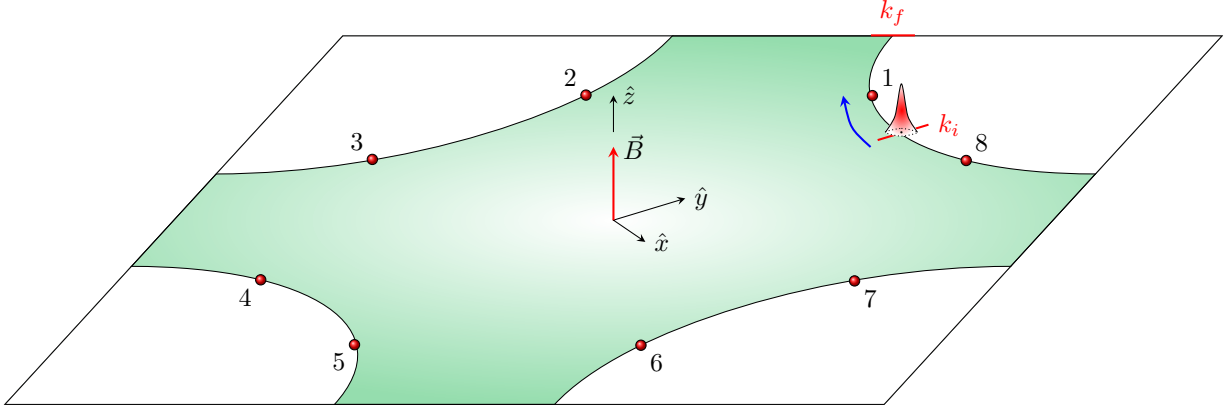


FIG. 5: Initial setup of the quasiparticle wavepacket. The initial wavepacket of a quasiparticle is placed at the boundary between segments 1 and 8 (k_i). In the presence of magnetic field applied in the z direction, the wavepacket moves along the Fermi surface towards hot spot 1. As it approaches hot spot 1, it slows down due to the momentum-dependent red shift.

quasiparticle even at zero temperature. However, the hot spots are a set of measure zero on the Fermi surface and do not affect the cyclotron period. For a quasiparticle localized at momentum \vec{k} , its time evolution is entirely determined by the kinetic action at that momentum. According to Eq. (15), the quasiparticle has Fermi velocity given by

$$\vec{v}_F(k) = \left(k \frac{\partial v_k}{\partial k} + v_k \right) \hat{x} + \hat{y} \quad (16)$$

when the Fermi velocity is measured with respect to the proper time τ defined at that momentum through $d\tau = \epsilon_t^0 dt$, where t represents the time associated with the bare frequency ω . Since the equation of quasiparticle at momentum k is entirely determined from the Fermi velocity and the proper time defined at that momentum, the equation of motion for the the wavepacket of a quasiparticle is given by the standard equation of motion[61],

$$\frac{d\vec{r}}{d\tau} = \vec{v}_F(k), \quad \frac{d\vec{k}}{d\tau} = -e \vec{v}_F(k) \times \vec{B}, \quad (17)$$

when written in terms of the local proper time coordinate τ , where $\vec{B} = B_0 \hat{z}$ is the magnetic field applied along the \hat{z} direction. B_0 is assumed to be weak so that it does not affect the renormalized coupling functions. To measure the cyclotron period in the lab frame, however, we need to recast the equations of motion in the bare time t ,

$$\frac{1}{\epsilon_t^0} \frac{d\vec{r}}{dt} = \left(k \frac{\partial v_k}{\partial k} + v_k \right) \hat{x} + \hat{y}, \quad \frac{1}{\epsilon_t^0} \frac{d\vec{k}}{dt} = -eB_0 \left[\hat{x} - \left(k \frac{\partial v_k}{\partial k} + v_k \right) \hat{y} \right], \quad (18)$$

where the effects of the curved spacetime are captured by the vielbein ϵ_t^0 . We consider quasiparticles on the Fermi surface, which allows us to focus on the equation of motion for the momentum along the Fermi surface.

Now let us proceed with the solutions. For $k_c < k_i$ ($k_i > \frac{\Lambda}{4v_0}$), there exists a region of Fermi surface near the zone boundary where the renormalization from spin fluctuations is negligible at energies below UV cutoff Λ . In this case, $T(k_i, 0; v_0)$ can be written as the sum of three intervals, $T(k_i, 0; v_0) = T(k_i, k_c; v_0) + T(k_c, k^*; v_0) + T(k^*, 0; v_0)$. $T(k_i, k_c; v_0)$ denotes the time that the quasiparticle spends in the region where the quantum correction from spin fluctuations is negligible and the hybrid spacetime is almost flat. $T(k_c, k^*; v_0)$ arises from the region with algebraically decaying $\epsilon_t^0(k)$. Finally, $T(k^*, 0; v_0)$ denotes the time that the quasiparticle spends in the very vicinity of the hot spot where the flow of the nesting angle modifies the spacetime geometry from the algebraic form. In the following, we compute each time interval one by one.

In the cold region with $k_c < k < k_i$, $\epsilon_t^0 \approx 1$ (see the third line for $\mathcal{V}_{F,k}$ in Eq. (12)). From $\frac{d\vec{r}}{dt} = v_0(0)\hat{x} + \hat{y}$, $\frac{d\vec{k}}{dt} = -eB_0(\hat{x} - v_0(0)\hat{y})$, one readily obtains

$$T(k_i, k_c; v_0) = \frac{k_i - k_c}{eB_0}. \quad (19)$$

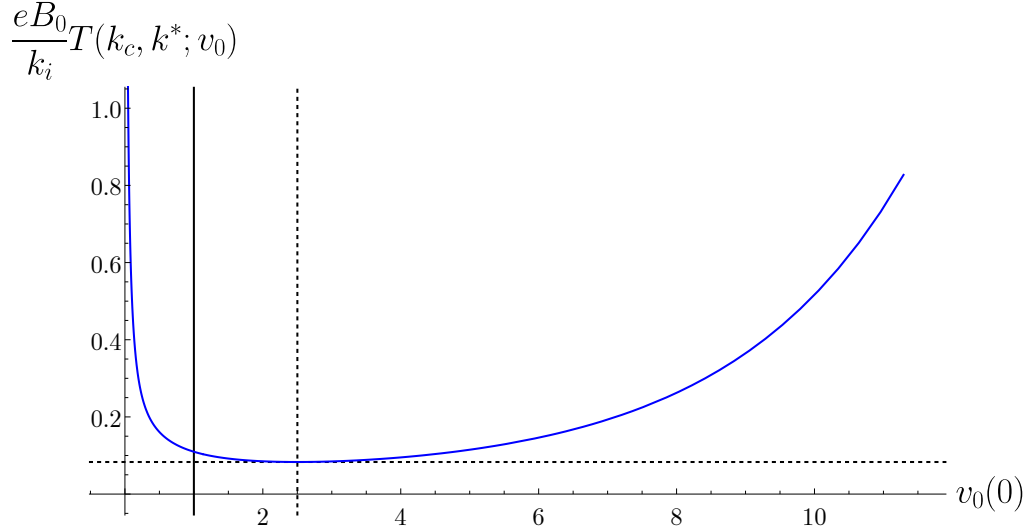


FIG. 6: The time that it takes for a quasiparticle to traverse from k_c to k^* plotted in the unit of $k_i/(eB_0)$ as a function of the bare nesting angle from $v_0 \approx 0.04$ to $v_0 \approx 11$ for the choice $k_i/\Lambda = 6$. The solid vertical line denotes the nesting angle ($v_0 \approx 1.13$) at which $\alpha_1 = 1$. The dashed lines mark the minimum of $T(k_c, k_i; v_0)$. The non-monotonic behaviour of $T(k_c, k_i; v_0)$ arises from the interplay between two effects : with increasing nesting angle, the size of the lukewarm region shrinks but the intensity of the red shift induced by quantum corrections is increased.

In $k^* < k < k_c$, the nesting angle can be still regarded as momentum-independent while the vielbein decays as $\epsilon_t^0 = (k/k_c)^{\alpha_1}$, following the second line in Eq. (12), where the exponent α_1 is determined from the bare nesting angle through Eqs. (9) and (13). The equations of motion become

$$\frac{d\vec{r}}{dt} = \left(\frac{k(t)}{k_c}\right)^{\alpha_1} (v_0(0)\hat{x} + \hat{y}), \quad \frac{d\vec{k}}{dt} = -eB_0 \left(\frac{k(t)}{k_c}\right)^{\alpha_1} (\hat{x} - v_0(0)\hat{y}), \quad (20)$$

where $k(t)$ denotes the x -component of $\vec{k}(t)$. Integrating $\frac{dk(t)}{dt} = -eB_0 \left(\frac{k(t)}{k_c}\right)^{\alpha_1}$ from k_c to k^* , we obtain

$$T(k_c, k^*; v_0) = \frac{k_c^{\alpha_1}}{eB_0} \int_{k^*}^{k_c} \frac{dk'}{k'^{\alpha_1}} = \frac{k_c}{(1-\alpha_1)eB_0} \left[1 - \left(\frac{k^*}{k_c}\right)^{1-\alpha_1} \right]. \quad (21)$$

$T(k_c, k^*; v_0)$ is plotted as a function of $v_0(0)$ in Fig. 6. This plot is obtained by substituting the expressions in Eqs. (13) and (9) in Eq. (21). For small nesting angle, $T(k_c, k^*; v_0)$ rapidly decreases with increasing $v_0(0)$. This is because the range of lukewarm region decreases with increasing nesting angle for a fixed Λ (see Eq. (A4) and Fig. 10). Furthermore, at larger nesting angles, even those electrons in the lukewarm region decouple from spin fluctuations at higher energy scales. Remarkably, $T(k_c, k^*; v_0)$ bounces back as $v_0(0)$ increases further. This non-monotonic behaviour is due to a competing effect that an increasing nesting angle has. At larger nesting angles, a reduction in the density of states of low-energy particle-hole excitations weakens the screening of interaction[23]. This makes the quantum-correction-induced red shift stronger for electrons close to the hot spots.

As the nesting angle increases, the portion of Fermi surface affected by spin fluctuations shrinks while electrons close to the hot spots are more significantly renormalized. The disparity in the strength of quantum correction in different parts of Fermi surface causes a more strongly curved spacetime at a large nesting angle. This is also reflected in the torsion that increases with increasing nesting angle as is shown in Fig. 4. The metric that becomes more singular at the hot spots with increasing nesting angle creates a possibility of realizing an analogous black hole horizon in momentum space. As α_1 approaches 1, the prefactor $\frac{k_c}{(1-\alpha_1)eB_0}$ in Eq. (21) diverges and $T(k_c, k^*; v_0)$ becomes

$$\lim_{\alpha_1 \rightarrow 1} T(k_c, k^*; v_0) = \frac{k_c}{eB_0} \log \left(\frac{k_c}{k^*} \right). \quad (22)$$

The leading small-angle expansion predicts that α_1 becomes 1 at $v_0 \approx 1.13$ for $N_c = 2$ and $N_f = 1$. Even though the small v_0 expansion is not valid for theories with $v_0 \sim 1$, here we proceed with the assumption that the qualitative

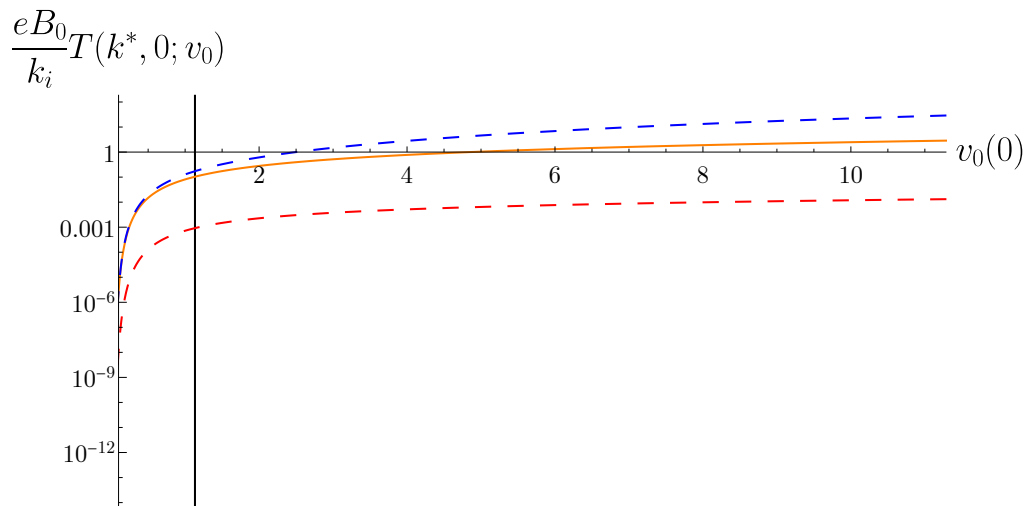


FIG. 7: The solid curve represents $T(k^*, 0; v_0)$ plotted as a function of $v_0(0)$. Two dashed lines that sandwich the solid curve are upper and lower bounds whose expressions can be obtained analytically (see text), which shows that $T(k^*, 0; v_0)$ is finite at all values of $v_0(0)$. The vertical line marks the nesting angle at which $\alpha_1 = 1$.

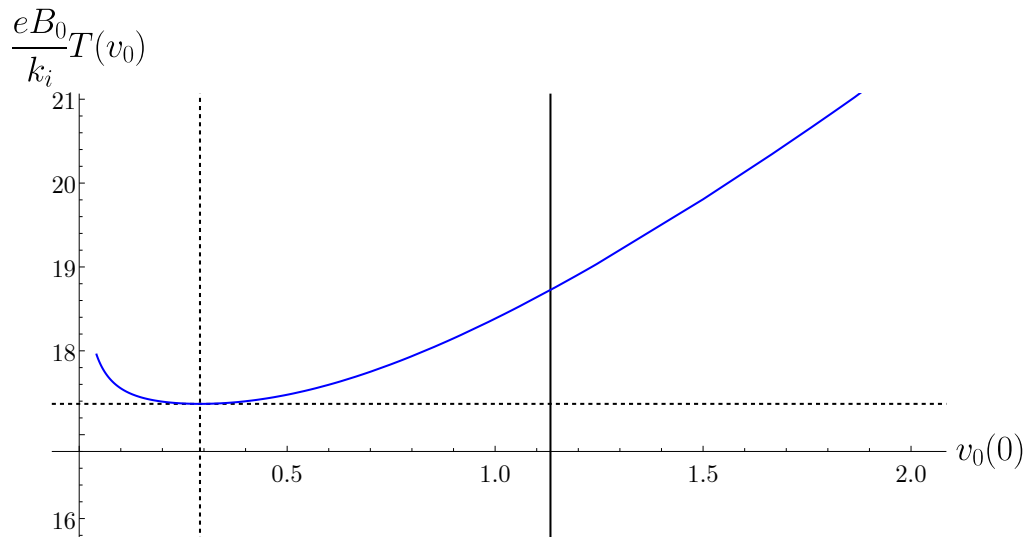


FIG. 8: The cyclotron period $T(v_0)$ plotted as a function of the bare nesting angle for $k_i/\Lambda = 6$. This plot is obtained by adding the times computed for Figs. 6 and 7. The solid vertical line denotes the nesting angle with $\alpha_1 = 1$, and the dashed lines mark the minimum of $T(v_0)$.

feature of the theory remains unchanged even at nesting angles that are not so small[45]. In this case, there may well be a critical nesting angle at which α_1 becomes 1 even if the actual critical value of v_0 differs from what is predicted from the small- v_0 expansion. The way the time interval depends on k^* in Eq. (22) is reminiscent of the logarithmic divergence in the time needed for a free-falling object to reach the horizon of the Schwarzschild black hole as measured by an asymptotic observer. This behaviour is analogous; nevertheless, it is not a coincidence. It is a consequence of the fact that at $\alpha_1 = 1$ the metric of a t and k slice of the hybrid spacetime in $k > k^*$ is conformally equivalent to that of the Schwarzschild black hole outside the horizon. For a review of the Schwarzschild metric and the time needed for a free-falling object to reach the horizon, see Appendix C. If k^* was zero, the cyclotron period would diverge and a quasiparticle would not be able to go through the hot spot for $\alpha_1 \geq 1$. In our case, the divergence is cut off by k^* because the momentum-spacetime geometry is modified from that of the Schwarzschild horizon for $k < k^*$ due to the flow of the nesting angle⁴.

⁴ For this reason, the geometry that emerges in the $\alpha_1 = 1$ limit is more a fuzzball[62] or a firewall[63] than a horizon with no ‘drama’.

For $0 < k < k^*$, the electrons stay coupled with spin fluctuations at energy scales that are low enough that one has to consider the flow of the nesting angle. This modifies the temporal vielbein from the algebraic form to a ‘super-logarithmic’ form⁵ in the first line of Eq. (12), $\epsilon_t^0 \approx \frac{1}{\nu(\ell_0)} \exp\left(-\sqrt{N_c^2 - 1} \frac{\sqrt{\ell_k^{(2L)} + \ell_0}}{\log \sqrt{\ell_k^{(2L)} + \ell_0}}\right)$,

where $\nu(\ell_0) = \exp\left\{-\sqrt{N_c^2 - 1} \text{Ei}(\log \sqrt{\ell_0})\right\}$. Because the nesting angle decreases in the vicinity of the hot spot, the quantum correction becomes weaker. As k approaches 0, ϵ_t^0 decreases to zero only as $e^{-\sqrt{\log 1/k}}$, which is slower than any power-law. This results in the time interval that remains finite even for $\alpha_1 \geq 1$, $T(k^*, 0; v_0) = \frac{\nu(\ell_0)}{eB_0} \int_0^{k^*} \exp\left(\sqrt{N_c^2 - 1} \frac{\sqrt{\ell_{k'}^{(2L)} + \ell_0}}{\log \sqrt{\ell_{k'}^{(2L)} + \ell_0}}\right) dk'$. Substitution $s = \sqrt{\ell_{k'}^{(2L)} + \ell_0}$ yields

$$T(k^*, 0; v_0) = \frac{\Lambda}{2v_0(0)} \frac{\nu(\ell_0)e^{\ell_0}}{eB_0} \int_{\sqrt{2\ell_0}}^{\infty} s \exp\left(-s^2 + \sqrt{N_c^2 - 1} \frac{s}{\log s}\right) ds. \quad (23)$$

It is hard to evaluate Eq. (23) exactly. But, we can bound it as $T^{(l)}(k^*, 0; v_0) < T(k^*, 0; v_0) < T^{(u)}(k^*, 0; v_0)$, where the lower bound is obtained by dropping $s/\log s$ in the exponent on the integrand of Eq. (23),

$$T^{(l)}(k^*, 0; v_0) = \frac{\nu(\ell_0)}{eB_0} k^*, \quad (24)$$

and the upper bound is obtained by using $\log s \approx \log \sqrt{2\ell_0}$,

$$T^{(u)}(k^*, 0; v_0) = \frac{\nu(\ell_0)}{eB_0} k^* \left[e^{\sqrt{N_c^2 - 1} \frac{\sqrt{2\ell_0}}{\log \sqrt{2\ell_0}}} + \sqrt{\frac{\pi(N_c^2 - 1)}{4}} e^{\frac{N_c^2 - 1}{4 \log^2 \sqrt{2\ell_0}} + 2\ell_0} \frac{1 + \text{erf}\left(\frac{\sqrt{N_c^2 - 1}}{2 \log \sqrt{2\ell_0}} - \sqrt{2\ell_0}\right)}{\log \sqrt{2\ell_0}} \right]. \quad (25)$$

Here, $\text{erf}(z) = \frac{2}{\sqrt{\pi}} \int_0^z e^{-t^2} dt$ is the error function. Fig. 7 shows $T(k^*, 0; v_0)$, $T^{(u)}(k^*, 0; v_0)$ and $T^{(l)}(k^*, 0; v_0)$ as functions of $v_0(0)$. The upper and lower bounds are direct plots of Eqs. (24) and (25). The solid line is obtained by numerically evaluating Eq. (23). This shows that $T(k^*, 0; v_0)$ is finite even for v_0 with $\alpha_1 \geq 1$. $T(k^*, 0; v_0)$ decreases with decreasing nesting angle. Especially, the sharp drop of $T(k^*, 0; v_0)$ in the small v_0 limit is due to the decrease of $k^* = \frac{\Lambda e^{-\ell_0}}{4v_0(0)}$ with decreasing v_0 (see Eq. (9)). The cyclotron period given by the sum of time lapse in each segment, $T(v_0) = 16 [T(k_i, k_c; v_0) + T(k_c, k^*; v_0) + T(k^*, 0; v_0)]$. $T(v_0)$ is plotted in Fig. 8. The non-monotonic behaviour of $T(v_0)$ as a function of v_0 is attributed to the non-monotonicity of $T(k_c, k^*; v_0)$ created by the increasing disparity in the strength of red shift across the Fermi surface with increasing v_0 .

So far, we have consider the zero-temperature limit in which the entire Fermi surface supports coherent quasiparticles except at the hot spots. Since electrons are decoupled from spin fluctuations away from the hot spots and all quantum effects that renormalize electrons have been fully incorporated into the renormalized couplings, the semi-classical description is valid at zero temperature. The hot spots, which is a set of measure zero, does not affect the cyclotron period of electrons. At non-zero temperatures, the hot spots become hot regions with a non-zero width proportional to temperature[19], and the contribution from the incoherent electrons can not be completely ignored. Nonetheless, at low temperatures, their contribution remains sub-leading for the cyclotron period compared to the contribution away from the segments of Fermi surface outside the hot regions. In particular, our conclusion on the non-monotonic behaviour of the cyclotron period as a function of the bare nesting angle, which originates from outside the hot region, remains robust as far as the size of hot regions remain much smaller than the remaining segments of Fermi surface. However, for completeness, we consider the effect of finite temperatures below based on the scaling analysis. We defer the more detailed study of the finite temperature correction from incoherent electrons to a future work.

In reality, the superconducting instability is inevitable in theories with non-zero bare nesting angle[19], and we have to consider a non-zero temperature to be in the normal state. In order to understand the transport in the hot region, one can not use the quasiparticle picture. At temperature \mathcal{T} that is higher than the energy scale below which the nesting angle flows ($\mathcal{T} > \Lambda e^{-\ell_0}$)⁶, the expression for the cyclotron period should be revised to $T(v_0) =$

The fact that the horizon is a special place is also seen from the fact that the torsion diverges at the hot spots (see Fig. 4). Another difference from the Schwarzschild horizon is that there is no interior of the black hole in our analogous horizon.

⁵ For this, we use $\text{Ei}(X) \approx \frac{e^X}{X}$ for $X \gg 1$.

⁶ In the small v_0 limit, the superconducting temperature is given by $T_c \sim \Lambda e^{-\frac{a}{\sqrt{v_0 \log 1/v_0}}}$ which is higher than the energy scale below which the nesting angle flows significantly, $\Lambda e^{-\frac{b}{v_0 \log(1/v_0)}}$, where a and b are constants independent of v_0 [19].

16 $[T(k_i, k_c; v_0) + T(k_c, k^\#; v_0) + T(k^\#, 0; v_0)]$. Here $T(k_i, k_c; v_0)$ in Eq. (19) is unchanged because we are still too far away from the hot spot ($k > k_c$.) $T(k_c, k^\#; v_0)$ is still given by Eq. (21) except that $k^\# \sim \mathcal{T}/v$ now represents the momentum cut-off scale associated with temperature \mathcal{T} ($\mathcal{T}/4v_0 > \Lambda e^{-\ell_0}/4v_0 = k^*$.) Finally, $T(k^\#, 0; v_0)$ represents the time that it takes for an incoherent electron pass through the hot region. In the small v_0 limit, the quasiparticle is only marginally destroyed and $T(k^\#, 0; v_0)$ can be estimated to be $T(k^\#, 0; v_0) \sim \frac{k^\#}{eB_0(k^\#/k_c)^{\alpha_1}}$. Here, the Fermi velocity has the form $(k^\#/k_c)^{\alpha_1}$ because the dynamics of the hot region at temperature \mathcal{T} now replaces the zero-temperature dynamics that previously contained the nesting angle profile ($k^\# > k^*$.)

In the zero-temperature superconducting state[19], one has to include the effect of the pair condensate to describe the dynamics of the Bogoliubov quasiparticles. Suppose that the ground state has the d-wave pairing[64] with a momentum-dependent pairing wavefunction Δ_k . For the physical case with $N_c = 2$ and $N_f = 1$, we need to add the following action for quasiparticles in segments 1 and 5,

$$S'^{1,5} = \sum_{\sigma, \sigma' = \uparrow, \downarrow} \int \frac{d\omega d^2k}{(2\pi)^3} \left\{ \psi_{1,\sigma}^*(\omega, \vec{k}) \Delta_k^{\sigma\sigma'} \psi_{5,\sigma'}^*(-\omega, -\vec{k}) + \psi_{5,\sigma}(-\omega, -\vec{k}) \Delta_k^{\dagger\sigma\sigma'} \psi_{1,\sigma'}(\omega, \vec{k}) \right\}, \quad (26)$$

where $\Delta_k^{\sigma\sigma'} = \Delta_k \epsilon^{\sigma\sigma'}$ with $\epsilon = \begin{pmatrix} 0 & 1 \\ -1 & 0 \end{pmatrix}$. The derivation of this equation can be found in Appendix D. Eqs. (11) and (26) can be combined into an action of a spinor field that represents Bogoliubov quasiparticles in the superconducting state,

$$S_{\text{kin}}^{1,5} + S'^{1,5} = \int \frac{d\omega d^2k}{(2\pi)^3} \bar{\Psi}(\omega, \vec{k}) \{ i\omega\Gamma^0 + i\mathcal{V}_{F,k}(v_k k_x + k_y)\Gamma^1 - i\Delta_k\Gamma^2 \} \Psi(\omega, \vec{k}), \quad (27)$$

where $S_{\text{kin}}^{1,5}$ are the terms of the kinematic action corresponding to electrons in hot spots 1 and 5, and $\Psi^T(\omega, \vec{k}) = (\psi_{1,\uparrow}(\omega, \vec{k}), \psi_{1,\downarrow}(\omega, \vec{k}), \psi_{5,\downarrow}^*(-\omega, -\vec{k}), -\psi_{5,\uparrow}^*(-\omega, -\vec{k}))$ is a 4-component spinor. $\bar{\Psi}(\omega, \vec{k}) = \Psi^\dagger(\omega, \vec{k})\Gamma^0$ with $\Gamma^0 = \sigma_y \otimes \mathbb{1}_2$, $\Gamma^1 = \sigma_x \otimes \mathbb{1}_2$, $\Gamma^2 = \sigma_z \otimes \mathbb{1}_2$ being 4×4 gamma matrices, where the first Pauli matrices act on the Nambu spinor basis and the second Pauli matrices act on the spin space. Using the same transform as in Eq. (14) for the Dirac spinor Ψ in the hybrid momentum-spacetime (t, r, k) , Eq. (27) can be written as

$$S_{\text{kin}}^{1,5} + S'^{1,5} = \int \frac{dk}{2\pi} \int dt dr |\epsilon| \bar{\Psi}(t, r, k) \{ \Gamma^0 \epsilon_0^t D_t + \Gamma^1 \epsilon_1^r D_r \} \Psi(t, r, k). \quad (28)$$

Here, the vielbein and the U(1) gauge field are unchanged, but the pairing term gives rise to a complex spin connection, $\omega_{t,02} = 4i\Delta_k$. It will be of interest to find geometric interpretation of physical observables in the superconducting state.

V. Conclusion and Outlook

In this paper, we show that the momentum-dependent quantum correction that dilates frequency of electron anisotropically on the Fermi surface gives rise to a curved momentum-spacetime for low-energy quasiparticles in the 2+1 dimensional antiferromagnetic quantum critical metal. The non-trivial dependence of the emergent geometry on the shape of the Fermi surface causes a non-monotonic dependence of the cyclotron frequency on the bare nesting angle of the Fermi surface. With increasing nesting angle, the stronger disparity in the strength of quantum correction in different parts of Fermi surface makes the momentum-dependent red shift more singular at the hot spots. This creates a possibility of realizing an analogous black hole horizon at the hot spots where the motion of quasiparticle tend to freeze beyond a critical bare nesting angle of the Fermi surface. However, this analogous horizon does not lead to a vanishing cyclotron frequency because the metric in the vicinity of the hot spots is modified by thermal effects above the superconducting transition temperature. Our prediction can be in principle tested through a measurement of the cyclotron frequency as a function of the nesting angle near the hot spots in one of those materials.

We close with some discussions and outlook:

- We note that it is not necessary to use the perspective of curved momentum-spacetime to understand how the cyclotron period depends on the bare nesting angle. One can attribute the momentum-dependent quantum effect either to the Fermi velocity or to the background geometry. In the non-geometric picture, one can explain the same physics by introducing a momentum-dependent Fermi velocity in a flat momentum-spacetime. However, the main advantage of the geometric perspective is a conceptual one. Even in the non-geometric picture, the

origin of the momentum-dependent Fermi velocity is the red shift that dilates the frequency in a momentum-dependent manner. What makes electrons slower near the hot spots is not a modification of the dispersion but the slowing down of their clocks from the perspective of electrons in the cold region. This makes it more natural to understand the dynamics of quasiparticles from the geometric perspective.

- Although we considered the example of antiferromagnetic quantum critical metal, the emergence of a curved momentum space is a general phenomenon in metals where quantum corrections depend strongly on momentum along the Fermi surface. In any quantum critical metal associated with an order parameter carrying a non-zero momentum such as charge density wave criticality, we expect that a similar curved momentum-spacetime will emerge near the hot spots. Conversely, there are quantum critical metals with cold spots at which there is an enhanced blue shift. In the Ising-nematic quantum critical metal, quantum corrections vanish at discrete points on the Fermi surface due to the form factor of the order parameter that changes sign around the Fermi surface. It would be interesting to understand the dynamics of electrons near the cold spots in terms of the emergent momentum-space geometry.
- In this paper, we mainly considered the zero temperature limit in which the quasiparticle description is valid almost everywhere on the Fermi surface. At finite temperatures, the contribution of the incoherent electrons in the vicinity of the hot spots is not negligible. It is of great interest to understand the dynamics of incoherent electrons in a more general setting. In particular, it is curious how a momentum-space geometry defined locally in the momentum space interplay with large angle scatterings that are non-local in the momentum space.
- In the present study, the momentum dependent red-shift is the primary mechanism by which the Fermi velocity acquires strong momentum dependence near the hot spots. In general, other effects, such as the renormalization of the fermion dispersion, can further renormalize the dynamics of electrons. In the antiferromagnetic quantum critical metal, its effect is sub-leading in the limit that the nesting angle is small. It would be of interest to find examples where a more general form of curved momentum-spacetime emerge from such quantum corrections.

A. The origin of the momentum-dependent coupling functions

In this appendix, we review the functional renormalization group flow that gives rise to the momentum-dependence for the coupling functions[19]. The power of the floating energy scale μ in front of each coupling function in Eq. (1) denotes its scaling dimension under the interaction driven scaling[57] that is exact in the limit that the nesting angle is small[23]. The four-fermion coupling function λ , which has scaling dimension -1 , should be included in the renormalizable theory because it is promoted to a marginal coupling with the help of the Fermi momentum[19]. On the contrary, quartic boson couplings are strictly irrelevant under the interaction-driven scaling and can be dropped in the low-energy theory[23]. The low-energy theory does not include the quadratic action of the boson either because the local kinetic term is irrelevant under the interaction driven scaling⁷. The absence of the bare boson kinetic term in the action gives us the freedom to rescale the boson field to tune the magnitude of the Yukawa coupling at the hot spots. The physics does not depend on this choice, but it is convenient to choose the normalization so that $g_{0,0} = \sqrt{\pi v_0}/2$. With this choice, the boson self-energy is ‘canonically’ normalized to

$$D(\mathbf{q}) = \frac{1}{|q_0| + c(|q_x| + |q_y|)}, \quad (\text{A1})$$

where

$$c = \sqrt{\frac{v_0}{8N_c N_f} \log\left(\frac{1}{v_0}\right)} \quad (\text{A2})$$

is the speed of the dressed collective mode that is entirely determined from the nesting angle at the hot spots[23]. We also have the freedom to choose the scale of frequency relative to momentum. We first follow Ref. [19] to choose the unit of frequency such that $V_{F,0} = 1$ at all scales⁸. Since the electrons at the hot spots receive quantum corrections down to the zero energy limit, keeping $V_{F,k} = 1$ in Eq. (5) at all μ requires a continuous redefinition of k_0 relative to the bare frequency as the energy scale is lowered. Since we are using one global clock according to which the electrons at the hot spots have a fixed velocity, cold electrons away from the hot spots appear to be moving faster with this choice of frequency unit.

The evolution of the momentum-dependent vertex function (See Eq. (5)) with decreasing μ defines the functional renormalization group flow of the coupling functions[19]. In the space of coupling functions, an *interacting* fixed point arises at

$$v_k = 0, \quad V_{F,k} = 1, \quad g_{k',k} = 0, \quad \lambda \begin{pmatrix} N_1 & N_2 \\ N_4 & N_3 \\ k_1 & k_2 \\ k_1+k_2-k_3 & k_3 \end{pmatrix}; \begin{pmatrix} \sigma_1 & \sigma_2 \\ \sigma_4 & \sigma_3 \end{pmatrix} = 0 \quad (\text{A3})$$

with $g_{k',k}^2/v_k = \pi/2$. Although the couplings vanish at the fixed point, quantum corrections remain non-trivial due to the vanishing nesting angle at the fixed point. The anomalous dimension of the boson is controlled by $g_{k',k}^2/v_k \sim O(1)$ and Eq. (A3) is far from the Gaussian fixed point. For theories with non-zero nesting angles at UV, the coupling functions undergo a non-trivial renormalization group flow as energy is lowered. At low energies, the coupling functions acquire momentum dependence under the functional renormalization group flow because quantum corrections depend on momentum along the Fermi surface. In this paper, we consider the case, where v_k and $V_{F,k}$ are independent of momentum at UV cutoff scale Λ : $v_k(\ell=0) = v_0(0)$ and $V_{F,k}(\ell=0) = 1$, where $\ell \equiv \log \Lambda/\mu$ is the logarithmic length scale. For different UV theories, the exact profiles of the renormalized coupling functions are different, but the part that is singular at the hot spots is universal[19].

In the small nesting angle limit, only the one-loop and two-loop fermion self-energy corrections are important for the quadratic action of electrons (Fig. 9(a)). If the external electron is right at a hot spot, the electron can be scattered to another hot spot by emitting virtual bosons with zero energy. Since all virtual particles can have zero energy in the loop, a logarithmic singularity arises for electrons at hot spots. If the external electron is away from hot spots, virtual particles are forced to carry a non-zero energy. The energy, which is proportional to the deviation of momentum away from the hot spot and the nesting angle, cuts off the infrared singularity as is illustrated in Fig. 9(b). Because of this, electrons away from hot spots become decoupled from spin fluctuations at sufficiently low energies. The crossover energy scales for the one-loop and two-loop fermion self-energy of the electron on the Fermi surface with momentum $k = k_N$ relative to the hot spots are given by

$$E^{(1L)} = 2cv_k |k|, \quad E^{(2L)} = 4V_{F,k}v_k |k|. \quad (\text{A4})$$

⁷ Physically, this implies that the two-point function of the boson is entirely determined by quantum corrections at low energies.

⁸ With this choice, $V_{F,k}$ at $k \neq 0$ represents the Fermi velocity measured in the unit of the Fermi velocity at the hot spots.

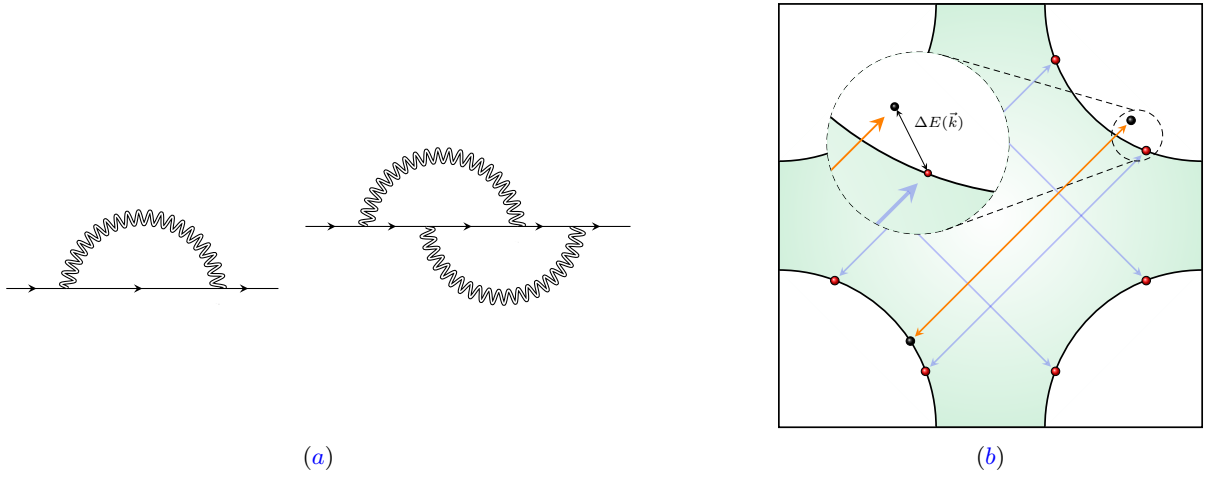


FIG. 9: (a) The leading quantum corrections that dress the quadratic action of electron in the limit that the nesting angle is small. The double wiggly line represents the fully dressed boson propagator obtained from the Schwinger-Dyson equation[23]. (b) The virtual electron created when an electron near hot spot 5 emits a boson with zero energy. If the electron is right at the hot spot 5, it is scattered onto the hot spot 8 on the Fermi surface. If the electron is away from the hot spot, it is scattered into a state away from the Fermi surface. The non-zero energy of the virtual particle (schematically called $\Delta E(\vec{k})$ here) cuts off the IR singularity of the self-energy. The form of $\Delta E(\vec{k})$ here depends on the channel of interaction. For example, for the one-loop fermion self-energy in (a) $\Delta E(\vec{k}) = E^{(1L)}$ and for the two-loop fermion self energy, $\Delta E(\vec{k}) = E^{(2L)}$ (See Eq. (A4).)

These crossover energy scales as functions of k are shown in Fig. 10. Each quantum correction turns off at energies far below $E_k^{(1L)}$ and $E_k^{(2L)}$, respectively. The logarithmic length scales associated with Eq. (A4) as

$$\ell_k^{(1L)} = \log\left(\frac{\Lambda}{2cv_k|k|}\right), \quad \ell_k^{(2L)} = \log\left(\frac{\Lambda}{4V_{F,k}v_k|k|}\right). \quad (\text{A5})$$

In the small v limit, the flow of couplings is negligible in $\ell_k^{(2L)} < \ell < \ell_k^{(1L)}$. Therefore, to the leading order in v , one can merge the two crossovers into one : for $\ell \gg \ell_k^{(2L)}$, both the one-loop and two-loop quantum corrections renormalize the Fermi velocity and the nesting angle, and for $\ell \ll \ell_k^{(2L)}$, both quantum corrections turn off. Because the quantum corrections that renormalize the coupling functions turn off at different energy scales at different momenta, the renormalized coupling functions end up acquiring non-trivial momentum dependences at low energies as is shown in Eqs. 7 and 8. Electrons closer to the hot spots remain coupled with spin fluctuations for a larger window of energy scales, and their Fermi velocity becomes smaller compared to electrons far away from hot spots. For the same reason, the electrons near the hot spots exhibit the stronger emergent nesting, that is the smaller renormalized nesting angle.

B. Spinors in curved spacetime

In this appendix, we review the background material for the theory of spinor in curved spacetimes. For concreteness, we consider four-dimensional spacetimes, but the discussion can be generalized to any dimension (for more details, see Ref. [65] for example). Suppose manifold M is endowed with metric $g_{\mu\nu}$. One can define a set of orthonormal basis that spans the space of one-forms through which the metric two-form can be written as

$$g_{\mu\nu}dx^\mu \otimes dx^\nu = \eta_{ab}\hat{\theta}^a \otimes \hat{\theta}^b, \quad (\text{B1})$$

where $\hat{\theta}^a = \mathbf{e}_\mu^a dx^\mu$ is the orthonormal basis, \mathbf{e}_μ^a is the vielbein and $\eta_{ab} = \text{diag}(-1, +1, +1, +1)$ ⁹. One can also introduce a set of vectors that is dual to $\{\hat{\theta}^a\}$ through the relation $\langle \hat{\theta}^a, \hat{e}_b \rangle = \delta_b^a$, where $\hat{e}_a = \mathbf{e}_a^\mu \partial_\mu$. The bases $\{\hat{e}_a\}$

⁹ For Euclidean signature, the Minkowskian metric η_{ab} is replaced with $\delta_{ab} = \text{diag}(+1, +1, +1, +1)$. In the following two paragraphs, we use the Einstein convention for the Greek and Latin indices.

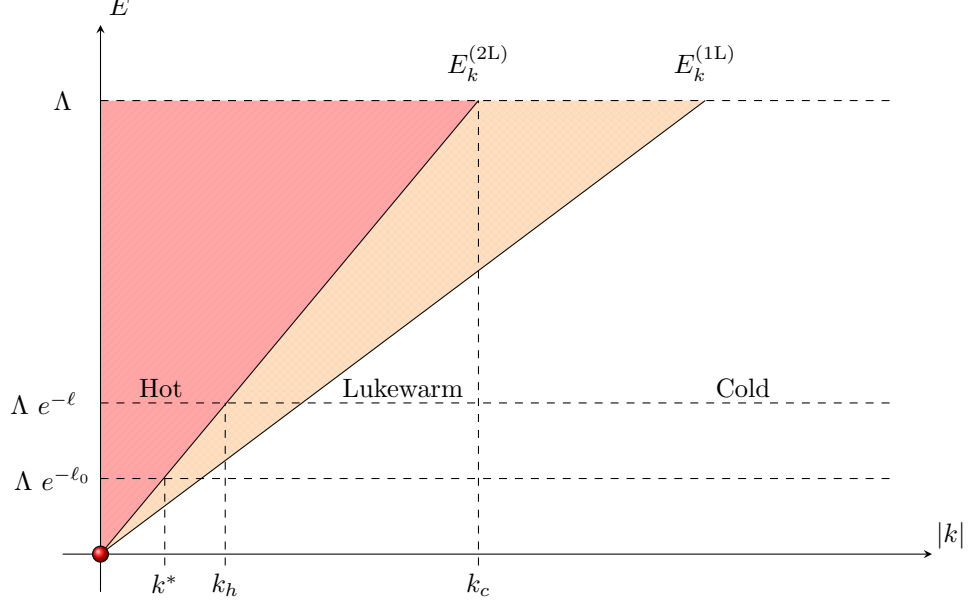


FIG. 10: Crossover energy scales associated with the two-loop fermion self-energy ($E_k^{(2L)}$) and the one-loop fermion self-energy ($E_k^{(1L)}$), respectively. At a small nesting angle, the flow of couplings between the two crossover energy scales is negligible, and one can use the approximation in which both quantum corrections turn off simultaneously below $E_k^{(2L)}$. At energy scales $\mu = \Lambda e^{-\ell}$, the momentum space is divided into three regions depending on the magnitude of $E_k^{(2L)}$ relative to μ and Λ . $\mu_0 \equiv \Lambda e^{-\ell_0}$ denotes the energy scale below which the flow of the nesting angle becomes important. In $k < k^*$, the shape of the Fermi surface is significantly renormalized.

and $\{\hat{\theta}^a\}$ are called the *non-coordinate bases*. There is clearly the freedom to rotate the orthonormal basis through the local Lorentz transformations. A relativistic fermion forms a spinor representation under this local Lorentz transformation. From the requirement that the action should be invariant under the local Lorentz transformation, the action for a Dirac spinor with mass m coupled to a gauge field $\mathcal{A}_\mu(x)$ is written as

$$\Gamma_\psi = \int_M \sqrt{|g|} d^4x \bar{\psi}(x) \gamma^c \mathbf{e}_c^\mu \left(\partial_\mu + \mathcal{A}_\mu(x) + \frac{i}{2} \omega_{\mu,ab} \Sigma^{ab} + m \right) \psi(x). \quad (\text{B2})$$

Here, $\sqrt{|g|} = |\mathbf{e}|$ with $\mathbf{e} = \det \mathbf{e}_\mu^a$. $\bar{\psi} = \psi^\dagger \gamma^0$, where the gamma matrices γ^a satisfy the Clifford algebra $\{\gamma^a, \gamma^b\} = 2\eta^{ab}$ that furnishes the spinor representation of local Lorentz transformation. $\Sigma^{ab} = \frac{i}{4} [\gamma^a, \gamma^b]$ is the generator of the local Lorentz transformations. The matrix-valued one form with elements $\omega_{\mu,ab} = (\omega_{ab})_\mu$ is the spin connection that acts as the gauge connection for the local Lorentz transformation. The connection one-form and the vielbein completely determines the torsion and curvature of the spacetime through the *Cartan structure equations*,

$$d\hat{\theta}^a + \omega_b^a \wedge \hat{\theta}^b = T^a, \quad (\text{B3a})$$

$$d\omega_b^a + \omega_c^a \wedge \omega_b^c = R_b^a, \quad (\text{B3b})$$

where d is the exterior derivative, \wedge is the wedge product, T^a is the torsion two-form and R_b^a is the curvature two-form. T^a and R_b^a are gauge covariant measures that characterize the geometry of the manifold M . The torsion measures the screw or twist on a frame when parallel transported along two directions in the manifold M . The curvature is a measure of the holonomy (gauge flux) acquired by a vector transported parallelly around a loop.

C. Schwarzschild Geodesics

In this appendix, we briefly review the Schwarzschild spacetime that describes a black hole and the motion of a free falling object (for a more complete review, see [66] for example). The Schwarzschild metric is an exact solution to

Einstein field equations, which describes the spacetime outside a static, neutral and spherically symmetric compact object. In the spherical coordinate, the line element for the Schwarzschild metric can be written as

$$ds^2 = \left(1 - \frac{r_s}{r}\right) c^2 dt^2 - \frac{dr^2}{1 - \frac{r_s}{r}} - r^2 d\theta^2 - r^2 \sin^2 \theta d\phi^2, \quad (\text{C1})$$

where M is the mass and c is the speed of light. t is the time coordinate that describes the proper time of an asymptotic observer who is at $r = \infty$, where r is the radial coordinate.

$$r_s = \frac{2GM}{c^2} \quad (\text{C2})$$

is the Schwarzschild radius, where G is the gravitational constant. When the radius of the compact object is smaller than r_s , it describes a black hole with an event horizon at $r = r_s$ inside of which the future light cone always points toward $r = 0$, and thus no escape. As the free falling object approaches the horizon from the outside, the lapse of its proper time is infinitely slowed down as compared to that of the proper time of an asymptotic observer. This gives rise to a critical slowdown of the motion of the free falling object as observed by the asymptotic observer. For an object that falls radially to the black hole at a fixed angle (say $\theta = \pi/2$ and $\phi = 0$), the geodesic equation of motion gives

$$t \sim \frac{r_s}{c} \log \left(\frac{\left| \sqrt{\frac{r}{r_s} + 1} \right|}{\left| \sqrt{\frac{r}{r_s} - 1} \right|} \right) \quad (\text{C3})$$

near the horizon. As r approaches r_s , t diverges logarithmically. This implies that the asymptotic observer will never see the passing of the free falling object across the horizon.

D. The pairing term for Bogoliubov quasiparticles

In this appendix we derive Eq. (26). We begin by writing the pairing interaction between electrons in segments 1 and 5 (See Fig. 1),

$$S_{4f}^{(1 \ 5)} = \frac{1}{4\mu} \sum_{\{\sigma_i\}} \int \frac{d\omega_p d\omega_k d\omega_q d^2p d^2k d^2q}{(2\pi)^9} \psi_{1,\sigma_1}^* \left(\omega_p + \frac{\omega_q}{2}, \vec{p} + \frac{\vec{q}}{2} \right) \psi_{5,\sigma_2}^* \left(-\omega_p + \frac{\omega_q}{2}, -\vec{p} + \frac{\vec{q}}{2} \right) \times \\ \lambda^{(1 \ 5); (\sigma_4 \ \sigma_3)}_{\left(\begin{smallmatrix} p+\frac{q}{2} & -p+\frac{q}{2} \\ k+\frac{q}{2} & -k+\frac{q}{2} \end{smallmatrix} \right)} \psi_{5,\sigma_3} \left(-\omega_k + \frac{\omega_q}{2}, -\vec{k} + \frac{\vec{q}}{2} \right) \psi_{1,\sigma_4} \left(\omega_k + \frac{\omega_q}{2}, \vec{k} + \frac{\vec{q}}{2} \right). \quad (\text{D1})$$

Here, λ is the four fermion coupling function generated from the critical spin fluctuations. The specific momentum-dependence of the coupling function is not important for us. The functional renormalization group analysis shows that the strongest attractive interaction is generated in the spin-singlet and d-wave channel, and the significant pairing interaction is generated not only for the electrons at the hot spots but also for electrons that are far away from the hot spots [19]. We are using the frequency defined in Eq. (10). Performing a Hubbard-Stratonovich transformation on the quartic interaction yields

$$e^{-S_{4f}^{(1 \ 5)}} = \int \mathcal{D}\Delta \mathcal{D}\Delta^* \exp \left\{ - \sum_{\{\sigma_i\}} \int \left(\prod_{l=p,q,k,q'} \frac{d\omega_l d^2l}{(2\pi)^3} \right) \left[\tilde{\Delta}^{\dagger \sigma_1 \sigma_2}_{(\omega_p, \vec{p}; \omega_q, \vec{q})} [-\bar{\lambda}]^{\sigma_1 \sigma_2; \sigma_3 \sigma_4}_{(\omega_p, \vec{p}, \omega_q, \vec{q}; \omega_k, \vec{k}, \omega_{q'}, \vec{q}')} \tilde{\Delta}^{\sigma_3 \sigma_4}_{(\omega_k, \vec{k}; \omega_{q'}, \vec{q}')} \right. \right. \\ - \psi_{1,\sigma_1}^* \left(\omega_p + \frac{\omega_q}{2}, \vec{p} + \frac{\vec{q}}{2} \right) \psi_{5,\sigma_2}^* \left(-\omega_p + \frac{\omega_q}{2}, -\vec{p} + \frac{\vec{q}}{2} \right) [-\bar{\lambda}]^{\sigma_1 \sigma_2; \sigma_3 \sigma_4}_{(\omega_p, \vec{p}, \omega_q, \vec{q}; \omega_k, \vec{k}, \omega_{q'}, \vec{q}')} \tilde{\Delta}^{\sigma_3 \sigma_4}_{(\omega_k, \vec{k}; \omega_{q'}, \vec{q}')} \\ \left. \left. - \tilde{\Delta}^{\dagger \sigma_1 \sigma_2}_{(\omega_p, \vec{p}; \omega_q, \vec{q})} [-\bar{\lambda}]^{\sigma_1 \sigma_2; \sigma_3 \sigma_4}_{(\omega_p, \vec{p}, \omega_q, \vec{q}; \omega_k, \vec{k}, \omega_{q'}, \vec{q}')} \psi_{5,\sigma_3} \left(-\omega_k + \frac{\omega_{q'}}{2}, -\vec{k} + \frac{\vec{q}'}{2} \right) \psi_{1,\sigma_4} \left(\omega_k + \frac{\omega_{q'}}{2}, \vec{k} + \frac{\vec{q}'}{2} \right) \right] \right\}, \quad (\text{D2})$$

where we use the matrix notation $[\bar{\lambda}]_{(\omega_p, \vec{p}; \omega_q, \vec{q}; \omega_k, \vec{k}; \omega_{q'}, \vec{q}')}^{\sigma_1 \sigma_2; \sigma_3 \sigma_4} = \frac{(2\pi)^3 \delta(\omega_p - \omega_{q'}) \delta^{(2)}(\vec{q} - \vec{q}')}{4\mu} \lambda \begin{pmatrix} 1 & 5 \\ 1 & 5 \end{pmatrix}; \begin{pmatrix} \sigma_1 & \sigma_2 \\ \sigma_4 & \sigma_3 \end{pmatrix}$ ¹⁰. Writing the static component of the order parameter with zero center of mass momentum as $\tilde{\Delta}_{(\omega_p, \vec{p}; \omega_q, \vec{q})}^{\sigma_1 \sigma_2} = (2\pi)^3 \delta(\omega_q) \delta^{(2)}(\vec{q}) \tilde{\Delta}_{(\omega_p, \vec{p})}^{\sigma_1 \sigma_2}$ and making a further transformation through

$$\Delta_{(\omega_p, \vec{p})}^{\sigma_1 \sigma_2} = \sum_{\sigma_3 \sigma_4} \int \frac{d\omega_k d^2 k}{(2\pi)^3} \frac{\lambda \begin{pmatrix} 1 & 5 \\ 1 & 5 \end{pmatrix}; \begin{pmatrix} \sigma_1 & \sigma_2 \\ \sigma_4 & \sigma_3 \end{pmatrix}}{4\mu} \tilde{\Delta}_{(\omega_k, \vec{k})}^{\sigma_3 \sigma_4}, \quad (\text{D3})$$

we obtain the pairing term for the Bogoliubov quasiparticles,

$$e^{-S_{4f} \begin{pmatrix} 1 & 5 \\ 1 & 5 \end{pmatrix}} = \int \mathcal{D}\Delta \mathcal{D}\Delta^* \exp \left\{ - \sum_{\{\sigma_i\}} \int \frac{d\omega_p d^2 p d\omega_k d^2 k}{(2\pi)^6} \Delta_{(\omega_p, \vec{p})}^{\sigma_1 \sigma_2} [\mathfrak{G}^{-1}] \begin{pmatrix} \sigma_1 & \sigma_2 \\ \sigma_4 & \sigma_3 \end{pmatrix} \Delta_{(\omega_k, \vec{k})}^{\sigma_3 \sigma_4} \right. \\ \left. - \sum_{\sigma_1, \sigma_2} \int \frac{d\omega_p d^2 p}{(2\pi)^3} \left[\psi_{1, \sigma_1}^* (\omega_p, \vec{p}) \Delta_{(\omega_p, \vec{p})}^{\sigma_1 \sigma_2} \psi_{5, \sigma_2}^* (-\omega_p, -\vec{p}) + \psi_{5, \sigma_1} (-\omega_p, -\vec{p}) \Delta_{(\omega_p, \vec{p})}^{\sigma_1 \sigma_2} \psi_{1, \sigma_2} (\omega_p, \vec{p}) \right] \right\}, \quad (\text{D4})$$

where $[\mathfrak{G}^{-1}] \begin{pmatrix} \sigma_1 & \sigma_2 \\ \sigma_4 & \sigma_3 \end{pmatrix} = 4\mu(2\pi)^3 \delta(0) \delta^{(2)}(\vec{0}) [-\lambda^{-1}] \begin{pmatrix} 1 & 5 \\ 1 & 5 \end{pmatrix}; \begin{pmatrix} \sigma_1 & \sigma_2 \\ \sigma_4 & \sigma_3 \end{pmatrix}$. Once the momentum-dependent pairing amplitude is determined from the saddle-point equation, it together with the vielbein sets the background spacetime on which the Bogoliubov quasiparticles propagate.

Acknowledgement

This research was supported by the Natural Sciences and Engineering Research Council of Canada. Research at the Perimeter Institute is supported in part by the Government of Canada through Industry Canada, and by the Province of Ontario through the Ministry of Research and Information.

-
- [1] D. Xiao, M.-C. Chang, and Q. Niu, *Reviews of Modern Physics* **82**, 1959 (2010).
 - [2] C. Crnkovic, *Classical and Quantum Gravity* **5**, 1557 (1988).
 - [3] J. Kowalski-Glikman, *International Journal of Modern Physics A* **28**, 1330014 (2013).
 - [4] J. Lee and R. M. Wald, *Journal of Mathematical Physics* **31**, 725 (1990), <https://doi.org/10.1063/1.528801>.
 - [5] A. Ashtekar, L. Bombelli, and O. Reula, in *Mechanics, Analysis and Geometry: 200 Years After Lagrange*, North-Holland Delta Series, edited by M. Francaviglia (Elsevier, Amsterdam, 1991) pp. 417–450.
 - [6] S. Davis and M. Foster, *SciPost Physics* **12**, 10.21468/scipostphys.12.6.204 (2022).
 - [7] B. Amorim, A. Cortijo, F. de Juan, A. Grushin, F. Guinea, A. Gutiérrez-Rubio, H. Ochoa, V. Parente, R. Roldán, P. San-Jose, J. Schiefele, M. Sturla, and M. Vozmediano, *Physics Reports* **617**, 1 (2016).
 - [8] Y. Wang, Z. Chi, and J. Liu, *Composite Structures* **258**, 113204 (2021).
 - [9] V. M. Pereira, A. C. Neto, H. Liang, and L. Mahadevan, *Physical review letters* **105**, 156603 (2010).
 - [10] J. Mao, S. P. Milovanović, M. Anđelković, X. Lai, Y. Cao, K. Watanabe, T. Taniguchi, L. Covaci, F. M. Peeters, A. K. Geim, Y. Jiang, and E. Y. Andrei, *Nature* **584**, 215 (2020).
 - [11] M. Vozmediano, M. Katsnelson, and F. Guinea, *Physics Reports* **496**, 109 (2010).
 - [12] A. Cortijo and M. A. Vozmediano, *Nuclear Physics B* **763**, 293 (2007).
 - [13] M. A. Wilde, M. Dodenhöft, A. Niedermayr, A. Bauer, M. M. Hirschmann, K. Alpin, A. P. Schnyder, and C. Pfleiderer, *Nature* **594**, 374 (2021).
 - [14] H. D. Scammell and M. S. Scheurer, *Phys. Rev. Lett.* **130**, 066001 (2023).
 - [15] J. Mitscherling and W. Metzner, *Phys. Rev. B* **104**, L201107 (2021).
 - [16] T. B. Smith, L. Pullasserri, and A. Srivastava, *Momentum-space gravity from the quantum geometry and entropy of Bloch electrons* (2021), [arXiv:2108.02216 \[cond-mat.mes-hall\]](https://arxiv.org/abs/2108.02216).
 - [17] T. Holder, *arXiv preprint arXiv:2111.07782* (2021).

¹⁰ The matrix elements of $\bar{\lambda}$ can be written as $\bar{\lambda}_{mn}$, where $m \equiv (\sigma_1 \sigma_2; \omega_p, \vec{p}; \omega_q, \vec{q})$ and $n \equiv (\sigma_3 \sigma_4; \omega_k, \vec{k}; \omega_{q'}, \vec{q}')$.

- [18] N. Marzari, A. A. Mostofi, J. R. Yates, I. Souza, and D. Vanderbilt, *Rev. Mod. Phys.* **84**, 1419 (2012).
- [19] F. Borges, A. Borissov, A. Singh, A. Schlief, and S.-S. Lee, *Annals of Physics* **450**, 169221 (2023).
- [20] T. Helm, M. V. Kartsovnik, I. Sheikin, M. Bartkowiak, F. Wolff-Fabris, N. Bittner, W. Biberacher, M. Lambacher, A. Erb, J. Wosnitzer, and R. Gross, *Phys. Rev. Lett.* **105**, 247002 (2010).
- [21] K. Hashimoto, K. Cho, T. Shibauchi, S. Kasahara, Y. Mizukami, R. Katsumata, Y. Tsuruhara, T. Terashima, H. Ikeda, M. A. Tanatar, H. Kitano, N. Salovich, R. W. Giannetta, P. Walmsley, A. Carrington, R. Prozorov, and Y. Matsuda, *Science* **336**, 1554 (2012).
- [22] T. Park, F. Ronning, H. Yuan, M. Salamon, R. Movshovich, J. Sarrao, and J. Thompson, *Nature* **440**, 65 (2006).
- [23] A. Schlief, P. Lunts, and S.-S. Lee, *Phys. Rev. X* **7**, 021010 (2017).
- [24] A. Abanov and A. V. Chubukov, *Phys. Rev. Lett.* **84**, 5608 (2000).
- [25] A. Abanov, A. V. Chubukov, and J. Schmalian, *Adv. Phys.* **52**, 119 (2003).
- [26] A. Abanov and A. Chubukov, *Phys. Rev. Lett.* **93**, 255702 (2004).
- [27] S. A. Hartnoll, D. M. Hofman, M. A. Metlitski, and S. Sachdev, *Phys. Rev. B* **84**, 125115 (2011).
- [28] E. Abrahams and P. Wölfe, *Proc. Natl. Acad. Sci.* **109**, 3238 (2012).
- [29] J. Lee, P. Strack, and S. Sachdev, *Phys. Rev. B* **87**, 045104 (2013).
- [30] V. S. de Carvalho and H. Freire, *Nuclear Physics B* **875**, 738 (2013).
- [31] A. A. Patel, P. Strack, and S. Sachdev, *Phys. Rev. B* **92**, 165105 (2015).
- [32] C. M. Varma, *Phys. Rev. Lett.* **115**, 186405 (2015).
- [33] S. A. Maier and P. Strack, *Phys. Rev. B* **93**, 165114 (2016).
- [34] C. M. Varma, W. J. Gannon, M. C. Aronson, J. A. Rodriguez-Rivera, and Y. Qiu, *Phys. Rev. B* **97**, 085134 (2018).
- [35] M. A. Metlitski and S. Sachdev, *Phys. Rev. B* **82**, 075128 (2010).
- [36] S. Sur and S.-S. Lee, *Phys. Rev. B* **91**, 125136 (2015).
- [37] S.-S. Lee, *Annu. Rev. of Condens. Matter Phys.* **9**, 227 (2018).
- [38] E. Berg, M. Metlitski, and S. Sachdev, *Science* **338**, 1606 (2012).
- [39] Z.-X. Li, F. Wang, H. Yao, and D.-H. Lee, *Science Bulletin* **61**, 925 (2016).
- [40] Y. Schattner, M. H. Gerlach, S. Trebst, and E. Berg, *Phys. Rev. Lett.* **117**, 097002 (2016).
- [41] M. H. Gerlach, Y. Schattner, E. Berg, and S. Trebst, *Phys. Rev. B* **95**, 035124 (2017).
- [42] Z.-X. Li, F. Wang, H. Yao, and D.-H. Lee, *Phys. Rev. B* **95**, 214505 (2017).
- [43] X. Wang, Y. Wang, Y. Schattner, E. Berg, and R. M. Fernandes, *Phys. Rev. Lett.* **120**, 247002 (2018).
- [44] E. Berg, S. Lederer, Y. Schattner, and S. Trebst, Monte carlo studies of quantum critical metals (2018), [arXiv:1804.01988](https://arxiv.org/abs/1804.01988).
- [45] P. Lunts, M. S. Albergo, and M. Lindsey, arXiv e-prints, arXiv:2204.14241 (2022), [arXiv:2204.14241](https://arxiv.org/abs/2204.14241) [cond-mat.str-el].
- [46] B. J. Ramshaw, S. E. Sebastian, R. D. McDonald, J. Day, B. S. Tan, Z. Zhu, J. B. Betts, R. Liang, D. A. Bonn, W. N. Hardy, and N. Harrison, *Science* **348**, 317 (2015).
- [47] J. Custers, P. Gegenwart, H. Wilhelm, K. Neumaier, Y. Tokiwa, O. Trovarelli, C. Geibel, F. Steglich, C. Pépin, and P. Coleman, *Nature* **424**, 524 (2003).
- [48] S. E. Sebastian, N. Harrison, E. Palm, T. P. Murphy, C. H. Mielke, R. Liang, D. A. Bonn, W. N. Hardy, and G. G. Lonzarich, *Nature* **454**, 200 (2008).
- [49] S. E. Sebastian, N. Harrison, and G. G. Lonzarich, *Reports on Progress in Physics* **75**, 102501 (2012).
- [50] A. Legros, K. W. Post, P. Chauhan, D. G. Rickel, X. He, X. Xu, X. Shi, I. Božović, S. A. Crooker, and N. P. Armitage, *Phys. Rev. B* **106**, 195110 (2022).
- [51] S. K. Goh, P. L. Alireza, L. E. Klintberg, T. Murphy, F. Nakamura, D. J. Singh, and M. Sutherland, *Quantum oscillations in the high pressure metallic state of CaRuO_4* (2012), [arXiv:1205.3045](https://arxiv.org/abs/1205.3045) [cond-mat.str-el].
- [52] N. Doiron-Leyraud, C. Proust, D. LeBoeuf, J. Levallois, J.-B. Bonnemaïson, R. Liang, D. A. Bonn, W. N. Hardy, and L. Taillefer, *Nature* **447**, 565 (2007).
- [53] J. Singleton, C. de la Cruz, R. D. McDonald, S. Li, M. Altarawneh, P. Goddard, I. Franke, D. Rickel, C. H. Mielke, X. Yao, and P. Dai, *Physical Review Letters* **104**, 10.1103/physrevlett.104.086403 (2010).
- [54] S. Badoux, W. Tabis, F. Laliberté, G. Grissonnanche, B. Vignolle, D. Vignolles, J. Béard, D. Bonn, W. Hardy, R. Liang, et al., *Nature* **531**, 210 (2016).
- [55] V. Grinenko, K. Iida, F. Kurth, D. V. Efremov, S.-L. Drechsler, I. Cherniavskii, I. Morozov, J. Hänisch, T. Förster, C. Tarantini, J. Jaroszynski, B. Maiorov, M. Jaime, A. Yamamoto, I. Nakamura, R. Fujimoto, T. Hatano, H. Ikuta, and R. Hühne, *Scientific Reports* **7**, 10.1038/s41598-017-04724-3 (2017).
- [56] M. Kimata, T. Terashima, N. Kurita, H. Satsukawa, A. Harada, K. Kodama, K. Takehana, Y. Imanaka, T. Takamasu, K. Kihou, C.-H. Lee, H. Kito, H. Eisaki, A. Iyo, H. Fukazawa, Y. Kohori, H. Harima, and S. Uji, *Physical Review Letters* **107**, 10.1103/physrevlett.107.166402 (2011).
- [57] S. Sur and S.-S. Lee, *Phys. Rev. B* **90**, 045121 (2014).
- [58] D. Dalidovich and S.-S. Lee, *Phys. Rev. B* **88**, 245106 (2013).
- [59] T. D. Stanescu, V. Galitski, and H. D. Drew, *Physical Review Letters* **101**, 10.1103/physrevlett.101.066405 (2008).
- [60] T. Senthil, On the mass enhancement near optimal doping in high magnetic fields in the cuprates (2014), [arXiv:1410.2096](https://arxiv.org/abs/1410.2096) [cond-mat.str-el].
- [61] N. Ashcroft and N. Mermin, *Solid State Physics* (Cengage Learning, 2011).
- [62] S. D. Mathur, *Fortsch. Phys.* **53**, 793 (2005), [arXiv:hep-th/0502050](https://arxiv.org/abs/hep-th/0502050).
- [63] A. Almheiri, D. Marolf, J. Polchinski, and J. Sully, *Journal of High Energy Physics* **2013**, 62 (2013).
- [64] D. J. Scalapino, E. Loh, and J. E. Hirsch, *Phys. Rev. B* **34**, 8190 (1986).

- [65] N. D. Birrell and P. C. W. Davies, [Quantum Fields in Curved Space](#), Cambridge Monographs on Mathematical Physics (Cambridge University Press, 1982).
- [66] R. Wald, [General Relativity](#) (University of Chicago Press, 2010).